Author Manuscript

Author Manuscript

Author Manuscript

Author Manuscript

HHS Public Access

Author manuscript

Acta Biomater. Author manuscript; available in PMC 2021 February 01.

Published in final edited form as:

Acta Biomater. 2020 February ; 103: 172–188. doi:10.1016/j.actbio.2019.12.024.

MECHANICAL AND STRUCTURAL CHANGES IN HUMAN THORACIC AORTAS WITH AGE

Majid Jadidi[1], **Mahmoud Habibnezhad**[2], **Eric Anttila**[1], **Kaspars Maleckis**[3,4], **Anastasia Desyatova**[3,4], **Jason MacTaggart**[3], **Alexey Kamenskiy**[3,4,*]

[1]Department of Mechanical and Materials Engineering, University of Nebraska-Lincoln, Lincoln, NE

[2]Department of Computer Science, University of Nebraska-Lincoln, Lincoln, NE

[3]Department of Surgery, University of Nebraska Medical Center, Omaha, NE

[4]Department of Biomechanics, University of Nebraska Omaha, Omaha, NE

Abstract

Aortic mechanical and structural characteristics have profound effects on pathophysiology, but many aspects of physiologic stress-stretch state and intramural changes due to aging remain poorly understood in human tissues. While difficult to assess *in vivo* due to residual stresses and pre-stretch, physiologic stress-stretch characteristics can be calculated using experimentally-measured mechanical properties and constitutive modeling. Mechanical properties of 76 human descending thoracic aortas (TA) from 13–78-year-old donors (mean age 51±18 years) were measured using multi-ratio planar biaxial extension. Constitutive parameters were derived for aortas in 7 age groups, and the physiologic stress-stretch state was calculated. Intramural characteristics were quantified from histological images and related to aortic morphometry and mechanics. TA stiffness increased with age, and aortas became more nonlinear and anisotropic. Systolic and diastolic elastic energy available for pulsation decreased with age from 30 to 8kPa and from 18 to 5kPa, respectively. Cardiac cycle circumferential stretch dropped from 1.14 to 1.04, and circumferential and longitudinal physiologic stresses decreased with age from 90 to 72kPa and from 90 to 17kPa, respectively. Aortic wall thickness and radii increased with age, while the density of elastin in the tunica media decreased. The number of elastic lamellae and circumferential physiologic stress per lamellae unit remained constant with age at 102±10 and 0.85±0.04kPa, respectively. Characterization of mechanical, physiological, and structural features in human aortas of different ages can help understand aortic pathology, inform the development of

[*]Correspondence and Reprints requests to: Alexey Kamenskiy, PhD, Department of Biomechanics, Biomechanics Research Building, University of Nebraska at Omaha, Tel: (402) 554-6346, akamenskiy@unomaha.edu.

Declaration of interests

The authors declare that they have no known competing financial interests or personal relationships that could have appeared to influence the work reported in this paper.

Publisher's Disclaimer: This is a PDF file of an unedited manuscript that has been accepted for publication. As a service to our customers we are providing this early version of the manuscript. The manuscript will undergo copyediting, typesetting, and review of the resulting proof before it is published in its final form. Please note that during the production process errors may be discovered which could affect the content, and all legal disclaimers that apply to the journal pertain.

Author Manuscript Author Manuscript Author Manuscript Author Manuscript

animal models that simulate human aging, and assist with designing devices for open and endovascular aortic repairs.

Graphical Abstract

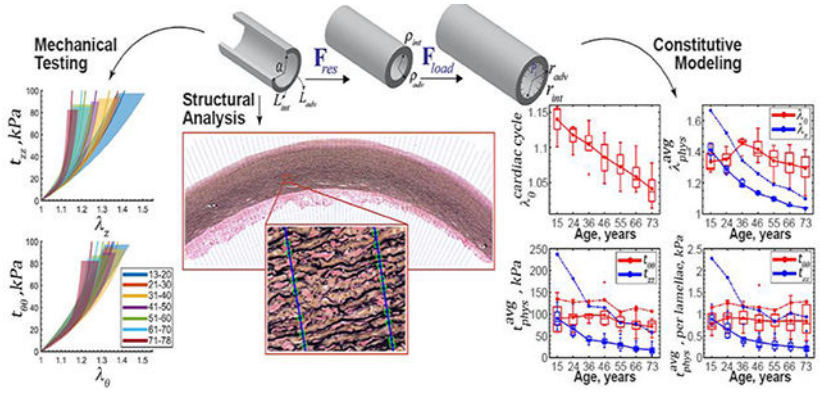

Keywords

thoracic aorta; human; mechanical properties; structural characteristics; elastin; physiologic state; mechanical stress; aging

1 INTRODUCTION

The aorta is the largest artery in the human body[1]. It distributes oxygenated blood to all organs and tissues, and acts as an elastic buffering chamber behind the heart that distends following ejection of blood from the left ventricle (LV) during systole, and then recoils after aortic valve closure[2,3]. This feature, known as the aortic Windkessel[4,5], provides a cushioning effect that protects the heart from pressure injury and helps perfuse the coronary arteries while creating a nearly continuous peripheral blood flow.

The aortic Windkessel function is inextricably linked to its elasticity, and stems primarily from the intramural aortic elastin[6] that is organized in the form of repeating sheets (called the elastic lamellae), the interlamellar elastic fibers, and thick radial elastin struts[2,7]. Most of the mature arterial elastin is produced during the perinatal period and stretches as the aorta grows in size[8,9], resulting in considerable tension and facilitating the Windkessel function. The number of elastic lamellae and the overall density of elastin in the aortic wall directly affect aortic elasticity[10–14] and define its Windkessel characteristics.

Aging, cyclic mechanical stress, proteolytic destruction, and other disease processes lead to degradation and fragmentation of elastic lamellae and fibers, which in combination with production and cross-linking of collagen and accumulation of proteoglycans and glycosaminoglycans, leads to aortic stiffening[15–17] and reduction of the Windkessel function. As higher ventricular forces are required to distend the stiffer aortic wall so it can continue to hold half of the LV stroke volume[5,18], this may result in increased systolic blood pressure[19–21], pulse wave velocity, and LV afterload[22–27], thereby causing LV hypertrophy, fibrosis, and changes in diastolic function that may eventually lead to

Author Manuscript Author Manuscript Author Manuscript Author Manuscript

contractile dysfunction and cardiomyopathy[14,19,29–34,20,22–28]. Distal to the heart, aortic stiffening enhances transfer of excessive, harmful pulsatile energy to the periphery, potentially altering blood flow characteristics in vital high-flow organs such as the brain and the kidneys, likely contributing to cognitive impairment and many forms of kidney disease[34,35,44–47,36–43].

While aortic stiffening is usually studied in the context of *in vivo* measurements such as pulse wave velocity or changes in aortic diameter during the cardiac cycle, many mechanical characteristics, like the intramural stresses, cannot be readily measured *in vivo* and require assessments using *ex vivo* tissue characterization and constitutive modeling. The assessment of the physiologic stress-stretch state is particularly complicated by the residual stresses[48–50] and longitudinal pre-stretch[51–53] that have profound effects on physiologic function[1,8], but cannot be measured without excising the artery.

In this study we have performed detailed mechanical characterization of human descending Thoracic Aortas (TA) in a wide range of ages, analyzed their physiologic stress-stretch state in relation to microstructure, and derived constitutive parameters for 4 commonly used constitutive models. This information can help improve understanding of basic aortic physiology and pathophysiology, and inform the development of animal models simulating human aging and disease. In addition, TA is one of the most commonly repaired aortic segments in trauma patients[54–56], many of whom are young and have compliant aortas with a strong Windkessel function. Presented analysis can help design new devices and materials for aortic repair in these patients.

2 METHODS

2.1 Aortic samples

Aortas were obtained by Live On Nebraska from 76 human subjects (age range 13 – 78 years, mean age 51 ± 18 years, 63% male, 97% Caucasian, none with aneurysmal disease) within 24 hours of death after obtaining consent from next in kin, transported in 0.9% phosphate-buffered saline at 4°C, and tested within 4 hours of procurement to preserve freshness. All samples were from the descending thoracic aorta, 1 cm distal to the left subclavian artery. Subject demographics and risk factors are summarized in Table 1.

Aortic rings were photographed in the *load-free* and radially-cut *stress-free* configurations to measure lengths of the intimal and adventitial surfaces (l_{int}, l_{adv}, L_{int}, L_{adv}) and the opening angle α (Figure 1) using a custom-written MATLAB program. Aortic wall thickness in the stress-free (H) and load-free (h) configurations was measured in 10 different locations along the aortic circumference to derive the average value for each specimen. All measurements were obtained by the same operator, and variability in aortic diameter and wall thickness values was 4±3%. Measurements of the circumference and opening angle allowed calculations of the *load-free* and *stress-free* radii ρ_{int}, ρ_{adv}, R_{int}, R_{adv} as[1,48,49]:

$$R_{int,adv} = \frac{L_{int,adv}}{2\pi - \alpha}, \quad \rho_{int,adv} = \frac{l_{int,adv}}{2\pi}. \qquad \text{Eq. 1}$$

Author Manuscript Author Manuscript Author Manuscript Author Manuscript

2.2 Planar Biaxial Testing

Planar biaxial tests were performed on 13 × 13 aortic specimens submerged into 0.9% phosphate-buffered saline at 37°C using a CellScale Biotester equipped with 5N loadcells[57,58]. Test axes were aligned with the longitudinal and circumferential directions of the aorta, and specimens were attached using rakes as previous studies demonstrated negligible shear in human TA specimens[15]. All samples were sprinkled with graphite markers to allow measurement of the deformation gradient, preloaded with 0.1N force, and subjected to 20 equibiaxial cycles of preconditioning until the force-stretch curves became repeatable. After that, a total of 21 stretch-controlled multi-ratio protocols were used to obtain sufficient data density for constitutive modeling. These protocols covered circumferential to longitudinal stretch ratios of 1:0.1 to 1:0.9 and 0.9:1 to 0.1:1 with 0.1 step, intermixed with three 1:1 equibiaxial protocols in the beginning, middle, and the end of the test sequence to ensure absence of tissue damage. Maximum stretch levels were selected for each specimen to ensure non-linearity in force-stretch curves while avoiding excessive stretch that can cause tissue damage. These stretches ranged from 1.09 to 1.5 depending on tissue compliance, and for most specimens corresponded to 1N force. All specimens were tested at 0.01 s^{-1} strain rate, and Cauchy stresses averaged through the thickness of the specimen were calculated as a function of the applied stretches in both the longitudinal (t_{zz}^{exp}) and the circumferential ($t_{\theta\theta}^{exp}$) directions as:

$$t_{zz}^{exp} = \frac{p_z}{hl_\theta}, \quad t_{\theta\theta}^{exp} = \frac{p_\theta}{hl_z},$$

where h is the deformed thickness of the specimen in the current configuration during the biaxial test, p_z and p_θ are the applied forces in the longitudinal and circumferential directions, and l_z and l_θ are the deformed lengths over which these forces act. Assuming incompressibility of the tissue during the biaxial test, the above formula can be written as a function of the biaxial stretches λ_z and λ_θ, thickness H in the reference configuration, and the undeformed lengths L_θ and L_z:

$$t_{zz}^{exp} = \lambda_z \frac{p_z}{HL_\theta}, \quad t_{\theta\theta}^{exp} = \lambda_\theta \frac{p_\theta}{HL_z}.$$

2.3 Constitutive models

Stress-stretch responses were used to determine constitutive parameters for the four invariant-based constitutive models commonly used to describe passive mechanical behavior of incompressible arteries[59,60]. Details of these models are summarized below.

2.3.1 The neo-Hookean model—This isotropic one-parameter model uses a linear function to describe the strain energy as:

Author Manuscript Author Manuscript Author Manuscript Author Manuscript

$$W = \frac{1}{2}\mu\left(I_{\boldsymbol{C}} - 3\right) + U(J), \qquad \text{Eq. 2}$$

where $I_{\boldsymbol{C}} = tr(\boldsymbol{C})$ is the first invariant of the right Cauchy-Green stretch tensor $\boldsymbol{C} = \boldsymbol{F}^T\boldsymbol{F}$, μ is the material parameter that needs to be determined from the experimental data, $J = \det\boldsymbol{F}$ is the third invariant of $\boldsymbol{C}$, and $U(J)$ is a purely volumetric contribution of strain energy function, which in the case of incompressible material defines Lagrange contribution.

2.3.2 The Demiray (Delfino) model—The Demiray (Delfino) model[61,62] also assumes isotropic response, but accounts for the stiffening of the aortic tissue by incorporating an exponential function:

$$W = \frac{D_1}{D_2}\left(\exp\left[\frac{D_2}{2}\left(I_{\boldsymbol{C}} - 3\right)\right] - 1\right) + U(J), \qquad \text{Eq. 3}$$

where, D_1 and D_2 are constitutive model parameters.

2.3.3 The classic two-fiber-family Holzapfel-Gasser-Ogden (HGO) model— Classic HGO has 4 constitutive parameters that allow to describe both the nonlinearity and the orthotropy of the tissue[63]. Though these parameters are phenomenological, they are usually related to the intramural aortic structure incorporating the contributions of the isotropic ground substance or elastin, and the two families of mechanically-equivalent collagen fibers that are helically oriented at the angle γ with the longitudinal direction:

$$\begin{aligned} W &= W_{gr} + \sum_{i=1}^{2} W_i + U(J), \\ W_{gr} &= \frac{C_{gr}}{2}\left(I_{\boldsymbol{C}} - 3\right), \qquad \text{Eq. 4} \\ W_i &= \frac{C_1^i}{2C_2^i}\left(e^{C_2^i\left\langle IV_{\boldsymbol{C}}^i - 1\right\rangle^2} - 1\right), \qquad i = 1, 2. \end{aligned}$$

Here $IV_{\boldsymbol{C}}^{1,2} = \boldsymbol{M}_{1,2} \cdot \left(\boldsymbol{C}\boldsymbol{M}_{1,2}\right)$ is the square of the stretch in the fiber direction $\boldsymbol{M}_{1,2}$, which in the absence of shear in the right Cauchy-Green stretch tensor $\boldsymbol{C}$, is equal to

$$IV_{\boldsymbol{C}}^{1,2} = \lambda_z^2 cos^2\gamma + \lambda_\theta^2 sin^2\gamma,$$

and C_{gr}, $C_1^{1,2}$, $C_2^{1,2}$, γ are the constitutive parameters determined from the experimental data. Assuming that the fibers are mechanically equivalent $C_1^1 = C_1^2$ and $C_2^1 = C_2^2$. Further, Macaulay brackets $\left\langle(\cdot)\right\rangle = \frac{1}{2}[(\cdot) + |(\cdot)|]$ are used to filter positive values so collagen fibers only contribute to stress during tension.

Author Manuscript Author Manuscript Author Manuscript Author Manuscript

2.3.4 The four-fiber family model—An extension of the HGO model that includes 4 instead of 2 families of fibers is usually used for arteries that demonstrate significant anisotropy[57,58,64–68]. It includes two additional families of fibers aligned with the longitudinal and circumferential directions which transforms the strain energy function to[69,70]:

$$W = W_{gr} + \sum_{i=1}^{4} W_i + U(J),$$
$$W_{gr} = \frac{C_{gr}}{2}(I_{\boldsymbol{C}} - 3), \qquad \text{Eq. 5}$$
$$W_i = \frac{C_1^i}{4C_2^i}\left(e^{C_2^i\left\langle IV_{\boldsymbol{C}}^i - 1\right\rangle^2} - 1\right), \qquad i = 1, 2, 3, 4,$$

Here $IV_{\boldsymbol{C}}^{3,4} = \boldsymbol{M}_{3,4} \cdot \left(\boldsymbol{C}\boldsymbol{M}_{3,4}\right)$, which in the absence of shear can be written as $IV_{\boldsymbol{C}}^3 = \lambda_\theta^2$ and $IV_{\boldsymbol{C}}^4 = \lambda_z^2$, i.e. the square of the stretch in the circumferential and longitudinal directions respectively.

The total Cauchy stress can then be calculated as the summation of the volumetric and isochoric parts:

$$\boldsymbol{t} = -p\boldsymbol{I} + \bar{\boldsymbol{t}} = -p\boldsymbol{I} + \overbrace{2\frac{\partial W}{\partial I_{\boldsymbol{C}}}\boldsymbol{B} + 2\sum_{i=1}^{4}\frac{\partial W}{\partial IV_{\boldsymbol{C}}^i}\boldsymbol{m}_i \otimes \boldsymbol{m}_i}^{\bar{\boldsymbol{t}}}, \qquad \text{Eq. 6}$$

where, $\boldsymbol{m_i} = \boldsymbol{F}\boldsymbol{M_i}$ and $\boldsymbol{M_i}$ is the unit vector aligned with the direction of fibers in the *reference* configuration, p is the Lagrange multiplier, and $\boldsymbol{B}$ is the left Cauchy-Green stretch tensor.

2.3.5 Determination of constitutive model parameters from the experimental data—Constitutive parameters for each of the 4 models were determined by minimizing each component of the error tensor $\boldsymbol{e}$ defined as

$$\boldsymbol{e} = \left|\boldsymbol{t}^{th}(\boldsymbol{F}, P) - \boldsymbol{t}^{exp}\right|,$$

where $\boldsymbol{t}^{th}$ is the theoretical Cauchy stress calculated using Eq. 6 and the experimentally-measured deformation gradient $\boldsymbol{F}$, and material parameter(s) P are defined by Eq. 2, Eq. 3, Eq. 4, and Eq. 5 for each of the constitutive models.

To ensure parameter uniqueness for the two- and four-fiber family models, we have performed a non-parametric bootstrap as described previously[57,64]. Briefly, it included 2000 iterations of random sampling and fitting, followed by the analysis of the probability distribution of each parameter to determine the global minimum.

Author Manuscript Author Manuscript Author Manuscript Author Manuscript

The quality of model fits to the experimental data was assessed using coefficient of determination R^2 calculated as:

$$R_\theta^2 = 1 - \frac{\sum_i^n \left(t_{\theta\theta}^{exp,i} - t_{\theta\theta}^{th,i}\right)}{\sum_i^n \left(t_{\theta\theta}^{exp,i} - t_{\theta\theta}^{exp,avg}\right)}, \quad R_z^2 = 1 - \frac{\sum_i^n \left(t_{zz}^{exp,i} - t_{zz}^{th,i}\right)}{\sum_i^n \left(t_{zz}^{exp,i} - t_{zz}^{exp,avg}\right)},$$
$$R^2 = \frac{R_\theta^2 + R_z^2}{2}.$$

Here i represents each experimental data point and R_θ^2 and R_z^2 are the coefficients of determination in the circumferential and longitudinal directions, respectively. Cauchy stress equations for all models are summarized in the Appendix 6.1.

In order to determine age-group-specific parameters for all constitutive models we followed a previously described approach[57,58,65] whereby the stress-controlled responses were first determined for all specimens using the constitutive model that produced the best fit to the experimental data; and then these curves were used to generate the average, and the 25th and 75th percentile stress-stretch curves for each age group. Constitutive model parameters were then determined by fitting to these curves, which produced age-group-specific values. This approach was used instead of mere averaging of the constitutive parameters between specimens which may produce an unpredictable result due to their interrelated nature.

2.3.6 Assessment of aortic anisotropy

Circumferential and longitudinal stretches at 25 kPa and 50 kPa equibiaxial stress levels were used to assess the anisotropy of the aortic tissues[67] as:

$$A_{25,50} = \frac{\lambda_z^{25,50} - \lambda_\theta^{25,50}}{0.5\left(\lambda_z^{25,50} + \lambda_\theta^{25,50}\right)}. \quad \text{Eq. 7}$$

Here A_{25} and A_{50} are the anisotropy ratios at 25 kPa and 50 kPa, respectively defined such that when the tissue is more compliant circumferentially than longitudinally, the anisotropy metric becomes negative.

2.4 Kinematics of residual and physiologic states

Aortic morphometry measurements and constitutive parameters determined from the experimental data were used to determine residual and physiologic stresses and stretches. Deformation gradients associated with transitions from the *stress-free* to the *load-free* and to the *in vivo loaded* states can be written as[1,59,63,71] $\boldsymbol{F}_{res} = diag\left[\frac{\partial \rho}{\partial R}, \mathrm{K}\frac{\rho}{R}, \lambda_\zeta\right]$, $\boldsymbol{F}_{load} = diag\left[\frac{\partial r}{\partial \rho}, \frac{r}{\rho}, \lambda_z^{in\ situ}\right]$ and $\boldsymbol{F}_{phys} = \boldsymbol{F}_{load}\boldsymbol{F}_{res} = diag\left[\frac{\partial r}{\partial R}, \frac{r}{R}\mathrm{K}, \lambda_\zeta \lambda_z^{in\ situ}\right]$, where R, ρ and r represent the *stress-free* cut ring, *load free* and *loaded* ring radii, respectively, $\mathrm{K} = \frac{2\pi}{2\pi - \alpha}$ is a measure of the opening angle, and λ_ζ and $\lambda_z^{in\ situ}$ are the residual and physiologic longitudinal stretches, respectively.

Author Manuscript Author Manuscript Author Manuscript Author Manuscript

Assuming incompressibility, one can find the *stress-free* and the *loaded* radii, R and r respectively, as a function of the *load-free* radius ρ:

$$R = \sqrt{R_{adv}^2 - \left(\rho_{adv}^2 - \rho^2\right)\mathrm{K}\lambda_\zeta}, \quad \text{Eq. 8}$$

$$r = \sqrt{r_{adv}^2 - \frac{\left(\rho_{adv}^2 - \rho^2\right)}{\lambda_z^{in\ situ}}}, \quad \text{Eq. 9}$$

where λ_ζ is assumed to be equal to 1[1]. The adventitial radius R_{adv} and the measure of the opening angle K in Eq. 8 and r_{adv} in Eq. 9 can be determined using the equilibrium equations derived from the balance of linear momentum, the boundary conditions of zero pressure on the adventitial surface and zero axial force in the *load-free* state, and the assumption of zero pressure on the adventitial surface in the *loaded* state[1,59,63,71] (see details in the Appendixes 6.2 and 6.3).

Since the *in situ* longitudinal stretch was not measured when the aortas were excised, it was calculated based on subject's age and the formula reported by Horny et al.[51]:

$$\lambda_z^{in\ situ} = 2.4016 \times \left(Age^{-0.1957}\right). \quad \text{Eq. 10}$$

Please note that this formula was obtained for the abdominal, not for the thoracic aorta which may have a somewhat different pre-stretch[72]. In the absence of measured longitudinal pre-stretch, several research teams have determined it as stretch at which axial tethering force and luminal pressure decouple ($\lambda_z^{decoupling}$) [58,73–75]. At $\lambda_z^{decoupling}$ the aorta experiences minimal change in axial force during the cardiac cycle which minimizes the axial work. Though our recent analysis of human femoropopliteal arteries demonstrated that calculated $\lambda_z^{decoupling}$ and measured $\lambda_z^{in\ situ}$ can be significantly different in young subjects[58], in the current study we have calculated aortic physiologic stress-stretch state using both metrics which allowed to assess the influence of pre-stretch on the results.

Physiologic stresses and stretches were calculated assuming *stress-free* state as a reference. The longitudinal stretch is then given by either the Eq. 10 or the condition of pressure-axial force decoupling, and the circumferential physiologic stretch can be calculated from

$$\lambda_\theta^{phys} = \frac{r}{R}\mathrm{K}.$$

Physiologic stresses corresponding to these stretches were then determined using the constitutive model that provided the best fit to the experimental data. Furthermore, we have calculated the physiologic circumferential stiffness as the change in the average circumferential physiologic stress between systole (120 *mmHg*) and diastole (80 *mmHg*) divided by the change in the average circumferential stretch[58]:

Author Manuscript Author Manuscript Author Manuscript Author Manuscript

$$E_\theta = \frac{t_{\theta\theta}^{phys,\,avg}(sys) - t_{\theta\theta}^{phys,\,avg}(dias)}{\lambda_\theta^{phys,\,avg}(sys) - \lambda_\theta^{phys,\,avg}(dias)}. \quad \text{Eq. 11}$$

Here $t_{\theta\theta}^{phys,\,avg}$ and $\lambda_\theta^{phys,\,avg}$ are the average through-thickness circumferential physiologic Cauchy stress and stretch calculated by integrating them over the current volume and dividing by the total current volume.

Strain energy W was calculated at diastole and systole to assess elastic potential available for pulsation, and the change in the average circumferential physiologic stretch during the cardiac cycle was calculated as:

$$\lambda_\theta^{cardiac\ cycle} = \frac{r^{sys}}{r^{dias}} \quad \text{Eq. 12}$$

2.5 Histological analysis

TA histology was evaluated in aortic specimens immediately adjacent to the biaxially-tested segments. Due to previously reported directional differences in elastic fiber and lamellae architecture[76,77], we have performed histological analysis using both transverse and longitudinal sections in each subject. All tissues were fixed in methacarn, dehydrated in 70% ethanol, embedded in paraffin, sectioned using a microtome, and stained with a Verhoeff-Van Gieson (VVG) stain. The stained sections were then scanned at 20 × resolution and used to characterize intramural elastin.

Histological analysis was performed in a semi-automated fashion using a custom-written application in C++ with OpenCV library. This application created a gray-scale image that contained only the elastin pixels, and the 6^{th} order polynomials were best-fit to the inner and outer boundaries of the medial layer. A total of 200 through-thickness lines where then drawn perpendicular to the aortic section (Figure 2), and the number of elastic lamellae were counted along each of these lines. The obtained results were then averaged producing mean and standard deviation counts of elastic lamellae in each histological section.

To focus on the elastic lamellae while avoiding thinner interlamellar fibers[78] and short radial elastic fibers[7], a minimum thickness of 1 μm, a minimum length of 50 μm, and a minimum distance of 1 μm between the lamellae were set for all images. The density of elastin in the entire medial layer was then determined by dividing the total number of elastin pixels by the number of total pixels in the tunica media. For each subject, measurements were obtained separately for the circumferential and longitudinal sections, and since longitudinal sections included three axial strips, data for those were averaged. Each image analyzed by the semi-automated algorithm was reviewed by an operator to ensure correctness, and a subset of 30 images was used to compare manual and automatic lamellae counts. The difference between these counts was on average 10±8%, which was typically smaller than the variation observed within the same histological section.

Author Manuscript Author Manuscript Author Manuscript Author Manuscript

2.6 Statistical analysis

Pearson correlation coefficient r was used to assess the strength of linear relation between continuous variables, with values closer to ±1 demonstrating stronger relations. Statistical significance of the observed correlations was assessed by testing the hypothesis of no correlation (i.e. the null hypothesis) against the alternative hypothesis of nonzero correlation using independent sample t-tests and utilizing the *corr* function of MATLAB. Values of $p < 0.05$ were considered statistically significant.

3 RESULTS

Figure 3 describes changes in aortic dimensions in *load-free* and *stress-free* configurations with age. Both the *stress-free* and the *load-free* thicknesses increased with age (r = 0.45, $p < 0.01$, and r = 0.31, $p < 0.01$, respectively), and the *stress-free* thickness was on average 18 ± 8% larger compared with the *load-free* state. Intimal and adventitial lengths of the *stress-free* radially-cut aortic rings increased with age (r = 0.73, $p < 0.01$, and r = 0.57, $p < 0.01$, respectively) while the opening angle decreased (r = −0.25, $p < 0.04$). In young aortas, the radial cut resulted in almost flat specimens (i.e. larger opening angles), with the slightly longer adventitial surface. In older TAs the radially-cut ring curved intima outward (Figure 3C), and intimal surface was on average 5 ± 5% longer than the adventitial. The inner and outer aortic radii in the *load-free* (r = 0.67 and r = 0.65) and *loaded* (r = 0.41 and r = 0.53) configurations increased with age ($p < 0.01$), and this increase was most substantial for <50-year-old aortas.

Figure 4 demonstrates longitudinal and transverse histological sections of several TAs from different age groups, and Figure 5 illustrates changes with age in the elastin content, the number of elastic lamellae, and thickness of the medial layer. The elastic lamellae were dense, continuous, and undulated in young aortas, while old aortas contained thinner, fragmented, and straighter elastic lamellae radially separated by larger distances.

Density of elastin in the medial layer decreased with age as assessed by both transverse (r = −0.55, $p < 0.01$) and longitudinal ((r = −0.55, $p < 0.01$) sections. The number of elastic lamellae did not change significantly with age ($p = 0.10$ transverse and $p = 0.06$ longitudinal) and on average was 105±9 and 100±10 as measured on transverse and longitudinal sections, respectively (Figure 5). Tunica media thickness measured in transverse sections slightly increased with age (r = 0.19), but the change was not statistically significant ($p = 0.10$). There was a significant correlation between the number of elastic lamellae and elastin density (r = 0.46, $p < 0.01$ transverse, r = 0.61, $p < 0.01$ longitudinal) and the number of elastic lamellae was higher in aortas with thicker medial layer (r = 0.51, $p < 0.01$ transverse, r =0.65, $p < 0.01$ longitudinal sections).

TA specimens stiffened with age, and the stress-stretch response became more nonlinear and anisotropic (Figure 6, Figure 7, Figure 8 and Figure 9). As displayed in Figure 9, circumferential stretch corresponding to 25 *kPa* stress did not change with age ($p = 0.96$) but stretch at the 50 *kPa* stress level decreased with age significantly (r = −0.26, $p = 0.02$), illustrating an increase in nonlinearity. In the longitudinal direction, reduction in stretch with age was significant at both the 25 *kPa* and the 50 *kPa* stress levels (r = −0.44, $p < 0.01$ at 25

Author Manuscript Author Manuscript Author Manuscript Author Manuscript

kPa, r = −0.75, $p < 0.01$ at 50 *kPa*) demonstrating that TAs stiffened faster longitudinally than circumferentially. Tissue anisotropy at 25 *kPa* stress decreased with age from 0.022 to −0.020, while at 50 *kPa* stress it changed from 0.031 to −0.050, and the change in sign indicates a reverse in anisotropy in older aortas that became more compliant circumferentially than longitudinally.

Constitutive parameters describing the mechanical behavior of TAs in 7 age groups are summarized in Table 2 and Table 3 for all 4 constitutive models. The neo-Hookean model did not provide a good fit ($R^2 > 0.83 \pm 0.07$) especially in the high stress domain, while both the Demiray (Delfino) and the two-fiber family HGO models portrayed the experimental data better ($R^2 > 0.92 \pm 0.10$ and $R^2 > 0.93 \pm 0.11$, respectively). The four-fiber family model had the overall best fit to all 19 different experimental protocols ($R^2 \geq 0.99 \pm 0.01$), and the quality of fit did not depend on age (Figure 6 (old TA) and Appendix Figure 12 (young and middle-aged TAs)).

Stress-stretch curves representing the average TA specimens in each age group along with the 25th and 75th percentiles are plotted in Figure 7. Constitutive parameters used to generate the average curves for each age group are summarized in Table 3, and parameters corresponding to the 25th and 75th percentiles as well as the softest and stiffest samples in each age group are included in the Appendix 6.4. Figure 8 displays the equibiaxial experimental curves for all TA specimens evaluated in this study.

Figure 10 demonstrates changes in the calculated physiologic stress-stretch state with age. During the cardiac cycle young TAs experienced 1.14 circumferential stretch, and old TAs stretched only 1.04 with intimal surface stretching more than adventitial (1.17 vs 1.12 in the young and 1.05 vs 1.03 in the old, p<0.01). Longitudinal pre-stretches $\lambda_z^{in\ situ}$ (r = −0.96, $p < 0.01$) and $\lambda_z^{decoupling}$ (r = −0.87, $p < 0.01$) decreased with age significantly from 1.41 to 1.04 and from 1.67 to 1.10, respectively, and $\lambda_z^{decoupling} > \lambda_z^{in\ situ}$ in all age groups (17% in young TAs and 6% in old TAs). Relative to the *stress-free* configuration, at 100 mmHg young TAs stretched 1.34 circumferentially, while old TAs stretched 1.29 (r = −0.29, $p < 0.01$), and both demonstrated very similar stretches at the intimal and adventitial surfaces.

Circumferential and longitudinal physiologic stresses determined using $\lambda_z^{in\ situ}$ decreased with age from 90 to 72 kPa and from 90 to 17 kPa, respectively. The same stresses calculated using $\lambda_z^{decoupling}$ also decreased with age from 134 to 106 kPa (circumferential) and from 237 to 58 kPa (longitudinal). On average, physiologic circumferential and longitudinal stresses calculated using $\lambda_z^{decoupling}$ were 35±6 kPa (33±6%) and 81±38 kPa (100±10%) higher than stresses calculated using $\lambda_z^{in\ situ}$.

Average circumferential physiologic stress per lamellae unit did not change significantly with age ($p > 0.5$) and was on average 0.85±0.04 kPa if determined using $\lambda_z^{in\ situ}$ and 1.19±0.07 kPa if determined using $\lambda_z^{decoupling}$. Longitudinal physiologic stress per lamellae

Author Manuscript Author Manuscript Author Manuscript Author Manuscript

unit decreased (r = −0.68, $p < 0.01$) from 0.9 to 0.2 kPa when using $\lambda_z^{in\ situ}$ and from 2.27 to 0.93 kPa (r = −0.43, $p < 0.01$) when using $\lambda_z^{decoupling}$.

As demonstrated in Figure 11, systolic and diastolic elastic energy available for pulsation decreased with age from 30 to 8 kPa and from 18 to 5 kPa, respectively (r = −0.8, $p < 0.01$) and their difference (i.e. elastic energy stored during cardiac cycle) also decreased with age from 12 to 3 kPa (r = −0.77, $p < 0.01$). Finally, the physiologic circumferential stiffness increased from 359 to 839 kPa (r = 0.42, $p < 0.01$).

4 DISCUSSION

Aortic stiffness plays an important role in pathophysiology, and increased central artery stiffness is associated with an increased risk of cardiovascular events, end-organ damage, dementia, and death[20,29,30,41]. Though often assessed with *in vivo* methods such as pulse wave velocity or measurements of diameter change over the cardiac cycle, many aspects of aortic mechanics that determine stiffness cannot be easily measured *in vivo* and require *ex vivo* characterization and constitutive modeling. For example, intramural stresses[79,80] depend on residual stresses and pre-stretch, and assessment of structural characteristics requires histological analysis. In this study we have characterized the mechanical and structural properties of human TAs using planar biaxial testing, constitutive modeling, and image analysis, and have demonstrated how they change with age. We have also derived the parameters for some of the most commonly used constitutive models, which can facilitate future computational studies designing new devices and materials for aortic repair.

Our experimental data demonstrate that human TAs stiffened with age, and their stress-stretch responses became more nonlinear and anisotropic with a switch in anisotropy towards higher compliance in the circumferential as opposed to the longitudinal direction by the age of 50 years. These results are in agreement with other studies[77,81,82] that also reported stiffening of major elastic and muscular arteries with age[57,66,83–85] due to degradation and fragmentation of elastic fibers and lamellae[67,86], accumulation and cross-linking of collagen[87–89] and proteoglycans, and formation of advanced glycation end-products[90]. They also agree with our previous mechanical tests[15] that demonstrated higher circumferential (as opposed to longitudinal) compliance of older human TAs, and a reverse result in the young aortas, although the latter was previously evaluated in a single TA specimen. Our current observations made with a much larger sample size confirm that TAs younger than 50 years old were more compliant longitudinally than circumferentially, but after the age of 50 years the anisotropy reversed towards higher circumferential compliance. Histologically, we have observed a somewhat higher elastin density in transverse as opposed to longitudinal aortic sections, which may contribute to these mechanical characteristics. Also of interest, a recent study[91] demonstrated higher longitudinal (as opposed to circumferential) compliance of porcine TAs which agrees well with the characteristics of young human aortas.

Author Manuscript Author Manuscript Author Manuscript Author Manuscript

Increased non-linearity and anisotropy of older aortas required more complex constitutive relations[64,68,69,92] to describe their behavior. While the neo-Hookean formulation did not provide a good fit for the majority of the aortic specimens, Demiray (Delfino) demonstrated reasonably good results, particularly for the younger more isotropic specimens, which makes this simple model attractive for computational simulations. Modeling of older more anisotropic and non-linear TAs may need to use the four-fiber family formulation. Since this model has twice as many constitutive parameters than the HGO, its use is associated with the additional effort of conducting multiple multi-ratio tests and performing subsequent non-parametric bootstrapping to study parameter uniqueness; however, these activities may be justified by the excellent portrayal of the experimental data with the four-fiber relation. For completeness, and to increase the utility of presented data, we have reported material parameters for all 4 considered models in all age groups along with the softest and stiffest samples in each group (see Appendix).

Changes in the mechanical properties with age were associated with the increase in TA diameter and wall thickness measured in both *load-free* and *stress-free* configurations. Diameter growth occurred at a faster rate in aortas <40 years old which agrees with previously reported analysis done using Computerized Tomography Angiography[93,94] and magnetic resonance imaging[95]. After residual stresses were released with a radial cut[1,48,49,96], young TAs demonstrated longer adventitial (as opposed to intimal) surfaces, but the result was reversed in older TAs that curved intima outward. This is consistent with previous experimental studies of human abdominal aortas[97] from >36 years old subjects that also curved intima outward. In addition to releasing the circumferential residual stresses, the radial cut appeared to also release some of the radial residual stresses as the aortic specimens were thicker in the *stress-free* configuration as opposed to the *load-free* state.

Morphological and mechanical differences between young and old TAs were associated with changes in the intramural elastin. Despite previously reported directional differences in elastic fiber and lamellae architecture[76,77], the number of lamellae we counted was consistent in both transverse and longitudinal histological sections (100±11 longitudinal and 105±9 circumferential), suggesting that our semi-automatic algorithm worked well in picking up major lamellae units instead of interlamellar elastic fibers and thick radial elastin struts[2,7]. The analysis further demonstrated that young TAs had continuous, thick, undulated, and tightly spaced elastic lamellae, and the overall density of elastin in the tunica media was 24.5±8.6%. Aging was associated with degradation, fragmentation, and straightening of the elastic lamellae, increase in interlamellar space, and an overall decrease in elastin density, although the number of elastic lamellae remained relatively constant at 102±10 across all age groups. An increase in the tunica media thickness and a constant number of lamellae resulted in the overall lower elastin density in older TAs (18.4±3.4%) and a larger interlamellar space. As suggested previously[98], this space can be filled with glycosaminoglycans that may increase the swelling pressure and contribute to higher propensity of older aortas to dissection. The straighter shape of elastic lamellae in older TAs may be an indication of vessel remodeling to a larger diameter, reduction in aortic Windkessel function (which was also reflected in the loss of elastic strain energy available for pulsation), and recruitment of collagen at lower values of stretch during pulsation which resulted in the overall increase in physiologic aortic stiffness.

Author Manuscript Author Manuscript Author Manuscript Author Manuscript

The number of elastic lamellae we counted in the TA (102±10 on average) agrees with most prior studies[10,13,99–101] but is larger than measured by Glagov and Wolinsky[10,13] (55–65 using four TA specimens), and the difference may be attributed to several factors. First, our data suggest a strong correlation between TA tunica media thickness and the number of elastic lamellae, but most of our TA specimens were much thicker (2.38±0.25 mm, likely due to lack of pressurization) and had larger diameter (19.18±2.7 mm on the intimal surface at 100 mmHg, likely due to more proximal location) than aortas evaluated by Glagov and Wolinsky (1.1 mm thickness and 18 mm diameter). In addition, the number of elastic lamellae appears to decrease from anterior to posterior aortic wall[99], but in our study we have measured the average count of lamellae by evaluating their number across the entire cross-section in 200 different locations.

Experimental data and constitutive modeling allowed to determine the circumferential stress per elastic lamellae unit that remained constant with age at 0.85±0.04 kPa (1.19±0.07 kPa if calculated using $\lambda_z^{decoupling}$), despite a decrease in physiologic circumferential stress from 90 to 72 kPa (134 to 106 kPa if using $\lambda_z^{decoupling}$). This confirms previous observations of Wolinsky and Glagov[13] and further refines their result. Conversely, longitudinal stress per lamellae unit decreased with age from 0.9 to 0.2 kPa (2.27 to 0.93 if using $\lambda_z^{decoupling}$), and so did the physiologic longitudinal stress (90 to 17 kPa for $\lambda_z^{in\ situ}$, and 237 to 58 kPa for $\lambda_z^{decoupling}$), likely due to a decrease in longitudinal pre-stretch (1.3 to 1.04 for $\lambda_z^{in\ situ}$ or 1.67 to 1.10 for $\lambda_z^{decoupling}$) with age. This demonstrates an important difference between circumferential and longitudinal stresses per lamellae unit and may suggest different pathophysiological mechanisms of their regulation.

Interestingly, despite the constant circumferential stress per lamellae unit, the overall physiologic circumferential stiffness increased with age from 359 to 839 kPa, with the most dramatic increase observed in >60-year-old TAs which is consistent with other studies[82]. The ability to store elastic energy during the cardiac cycle (i.e. the aortic Windkessel function) decreased with age 3.8-fold, and the circumferential cardiac cycle stretch reduced almost linearly from 1.14 to 1.05. Latter is in good agreement with previous *in vivo* evaluation using CT scans[102] that demonstrated 1.08±0.02 cyclic stretch in 41±7-year-old TAs, and 1.02±0.02 in 68±6-year-old TAs. Additionally, we have found the calculated circumferential stretch to be similar on the intimal and adventitial surfaces, which confirms previous findings of a uniform transmural stretch distribution due to presence of residual stresses[63,103–105].

It is interesting to compare physiologic stress-stretch characteristics in large elastic (i.e. the TA) and smaller muscular arteries, such as the human FPA, although these tissues were not obtained from the same human subjects. In a recent study[58] we have reported a decrease with age in physiologic circumferential and longitudinal FPA stresses from 48 to 32 kPa (i.e. 1.5-fold decrease) and from 117 to 24 kPa (i.e. 4.9-fold decrease), respectively. Circumferential FPA stretch (relative to the radially cut *stress-free* configuration) decreased from 1.26 to 1.11 (i.e. 2.4-fold), and longitudinal pre-stretch decreased from 1.53 to 1.11

Author Manuscript Author Manuscript Author Manuscript Author Manuscript

(i.e. 4.8-fold). Change in the FPA elastic strain energy during the cardiac cycle reduced with age from 2.3 to 0.4 kPa (5.8-fold), but the physiologic circumferential stiffness remained constant at 750 kPa.

Compared with the muscular FPA, elastic TA experienced higher circumferential (90–72 kPa) but lower longitudinal (90–17 kPa) physiologic stresses, and both reduced significantly with age (1.3-fold circumferential and 5.3-fold longitudinal). TAs also experienced larger circumferential stretch (1.34–1.29) but lower longitudinal pre-stretch (1.41–1.04,$\lambda_z^{in\ situ}$) than the FPAs, although circumferential stretch reduced with age slower than in the FPA (1.2 vs 2.4-fold), and the longitudinal pre-stretch reduced faster (10.3-fold). TAs used more elastic strain energy during pulsation, and reduction in this energy with age was slower in the TA than in the FPA (3.6-fold vs 5.8-fold). Finally, physiologic circumferential stiffness increased with age 2.3-fold, and became similar to the FPA values (750kPa) that remained relatively constant with aging. Together, these results suggest that large elastic arteries may adapt to aging differently than the smaller muscular arteries, yet both demonstrate common trends of reduced stresses and stretches with age, with greater changes occurring longitudinally.

It is also important to remember that this comparison was made using $\lambda_z^{in\ situ}$ determined for human abdominal, not thoracic aorta[51]. Though we have also calculated physiologic stresses using $\lambda_z^{decoupling}$, our FPA study[58] demonstrated that it can be significantly larger than $\lambda_z^{in\ situ}$ in young subjects, leading to much higher physiologic stresses. In our current analysis $\lambda_z^{decoupling}$ was on average 17% and 6% higher in young and old TAs than $\lambda_z^{in\ situ}$ reported by Horny et al[51], resulting in 35±6 kPa and 81±38 kPa higher physiologic stresses in the circumferential and longitudinal directions. This points to the importance of accurately measuring longitudinal pre-stretch in human TAs and the need to refine our current physiologic stress ranges when these data become available.

While the presented analysis describes the mechanical, morphological, physiological, and structural characteristics of human TAs of different ages, it is important to consider these results in the context of study limitations. First, we have not separated our specimens into layers and assumed homogenous mechanical properties despite obvious differences in the structure of the tunica intima, media, and adventitia. Although layer-specific studies of aortas are common[92,97,106] the effects of layer separation that disrupts the interfaces remains poorly understood. The difference in thickness after separation of the aortic layers[97] suggests that the structure of the aortic wall may be more complex than a mere summation of layers. Furthermore, aging and disease makes tissues highly inhomogeneous, even within the borders of one layer, which likely requires further compartmentalization.

The second limitation is related to the extraction of the elastic lamellae features from the two-dimensional histology images, and the challenges of distinguishing the elastic lamellae from the thinner interlamellar elastic fibers, and radial elastin struts[7]. Though 3D imaging, such as confocal and multiphoton microscopy[76,107–109] may be helpful, it was not available, and we have used threshold filters for lamellae thickness, length, and interlamellar

Author Manuscript Author Manuscript Author Manuscript Author Manuscript

distance to circumvent these issues. It is also important to note that in order to capture undulation of elastic lamellae in young TAs and contrast it with the straightened elastin in older aortas, we have not pressure-fixed our specimens. While helpful for understanding differences in lamellae undulation, this could have complicated the image analysis and may have potentially made it more prone to errors.

Third, in determining the physiologic stress-stretch state, we have not considered the influence of perivascular tethering[110]. Since cardiac cycle stretch calculated in our study was similar to the one measured using CTAs[102], we do not expect that perivascular tethering will have a major effect on the results.

Fourth, we have used normal values of blood pressure for all age groups, but older patients may have higher blood pressure, which may affect physiologic stress-stretch calculations. Since our aortic specimens were obtained from deceased human donors, blood pressure information was not available.

Finally, in our current analysis we have not considered the influence of gender or risk factors that may have significant effects on the morphological and mechanical characteristics[100,111], and may therefore affect the physiologic stress-stretch state. Although our current sample size did not allow us to perform this analysis while also controlling for age, we hope that these studies will be performed in the future. In the meantime, the presented data can help better understand changes in aortic physiology with age, inform the development of animal models that simulate human aging, and may help design devices for open and endovascular aortic repairs.

ACKNOWLEDGEMENTS

Research reported in this publication was supported in part by the National Heart, Lung, And Blood Institute of the National Institutes of Health under Award Numbers HL125736 and HL147128, and The U.S. Army Medical Research and Materiel Command (USAMRMC) under Award Number W81XWH-16-2-0034, Log 14361001. The authors also wish to acknowledge Live On Nebraska for their help and support, and thank tissue donors and their families for making this study possible.

6: APPENDICES

6.1 Stress Equations

The Cauchy stress relations for each of the four constitutive models considered in this study can be derived from the Eq. 6

$$\boldsymbol{t} = -p\boldsymbol{I} + \overline{\boldsymbol{t}} = -p\boldsymbol{I} + \overbrace{2\frac{\partial W}{\partial I}_{\boldsymbol{C}}\boldsymbol{B} + 2\sum_i \frac{\partial W}{\partial IV^i}_{\boldsymbol{C}}\boldsymbol{m}_i \otimes \boldsymbol{m}_i}^{\overline{\boldsymbol{t}}}.$$

The isochoric part of the stress tensor $\bar{\boldsymbol{t}}$ can be determined from the strain energy, and the Lagrange multiplier p can be calculated by applying the boundary conditions for each deformation. The Left Cauchy-Green stretch tensor $\boldsymbol{B}$ in the absence of shear can be written as

Author Manuscript Author Manuscript Author Manuscript Author Manuscript

$$\boldsymbol{B} = diag\left[\lambda_r^2, \lambda_\theta^2, \lambda_z^2\right]$$

where, λ_r, λ_θ and λ_z are the principal stretches in the radial, circumferential and longitudinal directions, respectively, and assuming incompressibility $\lambda_r = \frac{1}{\lambda_\theta \lambda_z}$.

6.1.1 The neo-Hookean model

The strain energy function for the neo-Hookean model is given by Eq. 2. Components of the isochoric part of the stress tensor are given by

$$\begin{aligned} \bar{t}_{rr} &= \mu\lambda_r^2, \\ \bar{t}_{\theta\theta} &= \mu\lambda_\theta^2, \\ \bar{t}_{zz} &= \mu\lambda_z^2. \end{aligned}$$

In planar biaxial testing, the radial component of the Cauchy stress tensor is equal to zero, and the Lagrange multiplier can be determined from

$$t_{rr} = -p + \bar{t}_{rr} = 0 \Rightarrow p = \bar{t}_{rr}.$$

The non-zero components of the Cauchy stress tensor are then given by

$$\begin{aligned} t_{\theta\theta} &= \mu\left(\lambda_\theta^2 - \frac{1}{\lambda_z^2\lambda_\theta^2}\right), \\ t_{zz} &= \mu\left(\lambda_z^2 - \frac{1}{\lambda_z^2\lambda_\theta^2}\right). \end{aligned} \qquad \text{Eq. 13}$$

6.1.2 The Demiray (Delfino) model—The strain energy function for the Demiary (Delfino) model is given by Eq. 3. Following Eq. 6, $\frac{\partial W}{\partial I_{\boldsymbol{C}}}$ is given by

$$\frac{\partial W}{\partial I_{\boldsymbol{C}}} = \frac{D_1}{2}\left(\exp\left[\frac{D_2}{2}\left(I_{\boldsymbol{C}} - 3\right)\right]\right),$$

and components of the isochoric part of the stress tensor can be calculated from

$$\begin{aligned} \bar{t}_{rr} &= D_1\left(\exp\left[\frac{D_2}{2}\left(I_{\boldsymbol{C}} - 3\right)\right]\right)\lambda_r^2, \\ \bar{t}_{\theta\theta} &= D_1\left(\exp\left[\frac{D_2}{2}\left(I_{\boldsymbol{C}} - 3\right)\right]\right)\lambda_\theta^2, \\ \bar{t}_{zz} &= D_1\left(\exp\left[\frac{D_2}{2}\left(I_{\boldsymbol{C}} - 3\right)\right]\right)\lambda_z^2. \end{aligned}$$

Author Manuscript Author Manuscript Author Manuscript Author Manuscript

Since $t_{rr} = 0$ during the planar biaxial experiment, the non-zero components of the Cauchy stress tensor are

$$t_{\theta\theta} = D_1\left(\exp\left[\frac{D_2}{2}(I_{\boldsymbol{C}} - 3)\right]\right)\left(\lambda_\theta^2 - \frac{1}{\lambda_z^2\lambda_\theta^2}\right)$$
$$t_{zz} = D_1\left(\exp\left[\frac{D_2}{2}(I_{\boldsymbol{C}} - 3)\right]\right)\left(\lambda_z^2 - \frac{1}{\lambda_z^2\lambda_\theta^2}\right) \quad \text{Eq. 14}$$

6.1.3 The classic two-fiber-family Holzapfel-Gasser-Ogden (HGO) model

The strain energy function for this model is given by Eq. 4 and following Eq. 6 one can find

$$\bar{t}_{rr} = c_{gr}\lambda_r^2 = c_{gr}\frac{1}{\lambda_z^2\lambda_\theta^2},$$

$$\bar{t}_{\theta\theta} = c_{gr}\lambda_\theta^2 + \sum_{i=1}^{2} 2c_1^i\left\langle IV_{\boldsymbol{C}}^i - 1\right\rangle e^{c_2^i\left(IV_{\boldsymbol{C}}^i - 1\right)^2}\lambda_\theta^2 sin^2\gamma,$$

$$\bar{t}_{zz} = c_{gr}\lambda_z^2 + \sum_{i=1}^{2} 2c_1^i\left\langle IV_{\boldsymbol{C}}^i - 1\right\rangle e^{c_2^i\left(IV_{\boldsymbol{C}}^i - 1\right)^2}\lambda_z^2 cos^2\gamma,$$

with

$$IV_{\boldsymbol{C}}^i = \lambda_z^2 cos^2\gamma + \lambda_\theta^2 sin^2\gamma, \qquad i = 1, 2$$

Assuming $t_{rr} = 0$ during the planar biaxial test, Cauchy stress components become

$$t_{\theta\theta} = c_{gr}\left(\lambda_\theta^2 - \frac{1}{\lambda_z^2\lambda_\theta^2}\right) + \sum_{i=1}^{2} 2c_1^i\left\langle IV_{\boldsymbol{C}}^i - 1\right\rangle e^{c_2^i\left(IV_{\boldsymbol{C}}^i - 1\right)^2}\lambda_\theta^2 sin^2\gamma,$$
$$t_{zz} = c_{gr}\left(\lambda_z^2 - \frac{1}{\lambda_z^2\lambda_\theta^2}\right) + \sum_{i=1}^{2} 2c_1^i\left\langle IV_{\boldsymbol{C}}^i - 1\right\rangle e^{c_2^i\left(IV_{\boldsymbol{C}}^i - 1\right)^2}\lambda_z^2 cos^2\gamma\,. \quad \text{Eq. 15}$$

Here $IV_{\boldsymbol{C}}^{1,2} = \boldsymbol{M}_{1,2}\cdot\left(\boldsymbol{C}\boldsymbol{M}_{1,2}\right)$ is the square of the stretch in the fiber direction $\boldsymbol{M}_{1,2}$, which in the absence of shear in the right Cauchy-Green stretch tensor $\boldsymbol{C}$, is equal to

$$IV_{\boldsymbol{C}}^{1,2} = \lambda_z^2 cos^2\gamma + \lambda_\theta^2 sin^2\gamma\,.$$

Author Manuscript Author Manuscript Author Manuscript Author Manuscript

6.1.4 The four-fiber family model

The strain energy function for this model is given by Eq. 5. Similar to the two-fiber family model

$$\bar{t}_{rr} = c_{gr}\lambda_r^2 = c_{gr}\frac{1}{\lambda_z^2\lambda_\theta^2},$$

$$\bar{t}_{\theta\theta} = c_{gr}\lambda_\theta^2 + c_1^3\left\langle\lambda_\theta^2 - 1\right\rangle e^{c_2^3\left(\lambda_\theta^2-1\right)^2}\lambda_\theta^2 + \sum_{i=1}^{2} c_1^i\left\langle IV_{\boldsymbol{C}}^i - 1\right\rangle e^{c_2^i\left(IV_{\boldsymbol{C}}^i-1\right)^2}\lambda_\theta^2 sin^2\gamma,$$

$$\bar{t}_{zz} = c_{gr}\lambda_z^2 + c_1^4\left\langle\lambda_z^2 - 1\right\rangle e^{c_2^4\left(\lambda_z^2-1\right)^2}\lambda_z^2 + \sum_{i=1}^{2} c_1^i\left\langle IV_{\boldsymbol{C}}^i - 1\right\rangle e^{c_2^i\left(IV_{\boldsymbol{C}}^i-1\right)^2}\lambda_z^2 cos^2\gamma,$$

and considering $t_{rr} = 0$

$$\begin{aligned} t_{\theta\theta} &= c_{gr}\left(\lambda_\theta^2 - \frac{1}{\lambda_z^2\lambda_\theta^2}\right) + c_1^3\left\langle\lambda_\theta^2 - 1\right\rangle e^{c_2^3\left(\lambda_\theta^2-1\right)^2}\lambda_\theta^2 \\ &+ \sum_{i=1}^{2} c_1^i\left\langle IV_{\boldsymbol{C}}^i - 1\right\rangle e^{c_2^i\left(IV_{\boldsymbol{C}}^i-1\right)^2}\lambda_\theta^2 sin^2\gamma, \\ t_{zz} &= c_{gr}\left(\lambda_z^2 - \frac{1}{\lambda_z^2\lambda_\theta^2}\right) + c_1^4\left\langle\lambda_z^2 - 1\right\rangle e^{c_2^4\left(\lambda_z^2-1\right)^2}\lambda_z^2 \\ &+ \sum_{i=1}^{2} c_1^i\left\langle IV_{\boldsymbol{C}}^i - 1\right\rangle e^{c_2^i\left(IV_{\boldsymbol{C}}^i-1\right)^2}\lambda_z^2 cos^2\gamma\,. \end{aligned} \qquad \text{Eq. 16}$$

6.2 Kinematics of residual and physiologic deformations

The *stress-free* (*reference*) configuration (Figure 1A) is defined in terms of cylindrical coordinates (R, Θ, Z) as

$$R_{int} \le R \le R_{adv},\ 0 \le \Theta \le 2\pi - \alpha,\ 0 \le Z \le L,$$

where R_{int}, R_{adv}, α and L are the inner and outer radii, opening angle, and the length of the *stress-free* arterial segment, respectively. The deformation gradient $\boldsymbol{F}_{res}$ takes this configuration into the *load-free* state geometrically defined as [1,59,63,71]

$$\rho_{int} \le \rho \le \rho_{adv},\ 0 \le \vartheta \le 2\pi,\ 0 \le \zeta \le \xi,$$

where

Author Manuscript Author Manuscript Author Manuscript Author Manuscript

$$\rho = \rho(R),\ \vartheta = \frac{2\pi}{2\pi - \alpha}\Theta, \zeta = \lambda_\zeta Z.$$

In cylindrical coordinates $\boldsymbol{F}_{res}$ is then given by

$$\boldsymbol{F}_{res} = diag\left[\frac{\partial\rho}{\partial R}, \frac{\rho}{R}\frac{\partial\vartheta}{\partial\Theta}, \frac{\partial\zeta}{\partial Z}\right] = diag\left[\lambda_\rho, \lambda_\vartheta, \lambda_\zeta\right],$$

where λ_ρ, λ_ϑ and λ_ζ are the radial, circumferential and longitudinal residual stretches respectively, with λ_ϑ given by

$$\lambda_\vartheta = \frac{\rho}{R}\mathrm{K} \qquad \text{Eq. 17}$$

and $\mathrm{K} = \frac{2\pi}{2\pi - \alpha}$ is a measure of the circumferential opening angle. Assuming incompressibility, one can write

$$\rho_{adv}^2 - \rho_{int}^2 = \frac{1}{\mathrm{K}\lambda_\zeta}\left(R_{adv}^2 - R_{int}^2\right),$$

and similarly

$$\rho_{adv}^2 - \rho^2 = \frac{1}{\mathrm{K}\lambda_\zeta}\left(R_{adv}^2 - R^2\right). \qquad \text{Eq. 18}$$

By substituting R form Eq. 18 in Eq. 17, the circumferential residual stretch λ_ϑ can be calculated at each point through thickness as a function of ρ, ρ_{adv}, K, λ_ζ.

Further, deformation $\boldsymbol{F}_{load}$ takes the *load-free* configuration to the *loaded* configuration which in cylindrical coordinates is defined as

$$r_{int} \le r \le r_{adv},\ 0 \le \theta \le 2\pi,\ 0 \le z \le l,$$

where

$$r = r(\rho),\ \theta = \vartheta,\ z = \lambda_z\zeta.$$

$\boldsymbol{F}_{load}$ is given by

$$\boldsymbol{F}_{load} = diag\left[\frac{\partial r}{\partial\rho}, \frac{r}{\rho}\frac{\partial\theta}{\partial\vartheta}, \frac{\partial z}{\partial\zeta}\right] = diag\left[\lambda_r, \lambda_\theta, \lambda_z\right],$$

in which $\lambda_\theta = \frac{r}{\rho}$ is the circumferential stretch. Assuming incompressibility, similar to Eq. 18 one can write

Author Manuscript Author Manuscript Author Manuscript Author Manuscript

$$r_{adv}^2 - r^2 = \frac{1}{\lambda_z}\left(\rho_{adv}^2 - \rho^2\right), \quad \text{Eq. 19}$$

and find r as a function of ρ, ρ_{adv} and λ_z.

The total deformation gradient that the artery experiences *in vivo* is then given by

$$\boldsymbol{F}_{phys} = \boldsymbol{F}_{load}\boldsymbol{F}_{res},$$

and the circumferential stretch is calculated from

$$\lambda_\theta^{phys} = \lambda_\vartheta \lambda_\theta = \frac{\rho}{R}\mathrm{K} \times \frac{r}{\rho} = \frac{r}{R}\mathrm{K} \quad \text{Eq. 20}$$

6.3 Equilibrium and boundary conditions

The total Cauchy stress in (i.e. $\boldsymbol{t} = -p\boldsymbol{I} + \bar{\boldsymbol{t}}$) contains both the volumetric and the isochoric parts[1]. Constitutive parameters define the isochoric stress tensor $\bar{\boldsymbol{t}}$, but the volumetric component $-p\boldsymbol{I}$ needs to be determined from the equilibrium and boundary conditions for each deformation.

Assuming quasi-static motions, in the absence of body forces, for each of the residual and physiologic deformations the equilibrium equation is

$$div\, \boldsymbol{t} = 0, \quad \text{Eq. 21}$$

where *div* represents the spatial divergence. The above equation can be used to find the Lagrange multiplier p in Eq. 6, along with the unknown stretches. In the *load-free* configuration, the only non-trivial component of Eq. 21 is

$$div\, \boldsymbol{t} = 0 \;\Rightarrow\; \frac{\partial t_{\rho\rho}}{\partial \rho} + \frac{t_{\rho\rho} - t_{\vartheta\vartheta}}{\rho} = 0.$$

Integrating the above equation along the radial direction, and considering that $t_{\rho\rho}$ is only a function of radius ρ, one can write

$$t_{\rho\rho}(\rho) = \left(\int_{\rho_{int}}^{\rho} \frac{t_{\vartheta\vartheta} - t_{\rho\rho}}{\rho} d\rho\right) + t_{\rho\rho}\left(\rho_{int}\right) = \left(\int_{\rho_{int}}^{\rho} \frac{\left(-p + \bar{t}_{\vartheta\vartheta}\right) - \left(-p + \bar{t}_{\rho\rho}\right)}{\rho} d\rho\right) + t_{\rho\rho}\left(\rho_{int}\right).$$

Assuming $t_{\rho\rho}(\rho_{int}) = 0$ this further simplifies to

$$t_{\rho\rho}(\rho) = \int_{\rho_{int}}^{\rho} \frac{\bar{t}_{\vartheta\vartheta} - \bar{t}_{\rho\rho}}{\rho} d\rho\,. \quad \text{Eq. 22}$$

Author Manuscript Author Manuscript Author Manuscript Author Manuscript

The Lagrange multiplier can then be calculated at each point through aortic thickness by substituting $t_{\rho\rho}$ into Eq. 6, i.e.

$$p(\rho) = \bar{t}_{\rho\rho} - t_{\rho\rho}.$$

In addition, since axial force vanishes in the *load-free* configuration due to release of longitudinal pre-stretch, the axial global equilibrium can be written as[1]

$$F_{\zeta} = 2\pi \int_{\rho_{int}}^{\rho_{adv}} t_{\zeta\zeta}\rho d\rho = 0, \quad \text{Eq. 23}$$

where F_{ζ} denotes the axial force in the *load-free* state.

Eq. 22 and Eq. 23 combined with the boundary condition $t_{\rho\rho}(\rho_{adv}) = 0$ are then solved together to calculate the outer (adventitial) radius of the cut ring R_{adv} and the opening angle α in the *stress-free* state.

Similar to Eq. 22, for the *loaded* configuration one can write

$$t_{rr}(r) = \int_{r_{int}}^{r} \frac{\bar{t}_{\theta\theta} - \bar{t}_{rr}}{r} dr - P_{luminal}, \quad \text{Eq. 24}$$

where $P_{luminal}$ is the internal luminal pressure, and the Lagrange multiplier in this state is determined according to

$$p(r) = \bar{t}_{rr} - t_{rr}.$$

Furthermore, assuming no pressure on the outer surface of the aorta one can find

$$t_{rr}(r_{adv}) = \int_{r_{int}}^{r_{adv}} \frac{\bar{t}_{\theta\theta} - \bar{t}_{rr}}{r} dr - P_{luminal} = 0,$$

which can be used to find the outer (adventitial) radius r_{adv} in the *loaded* state.

6.4 Quality of fit for different constitutive models

Figure 12 illustrates the quality of fit to the experimental data for 4 different constitutive models in a representative young (14-year-old) and middle-aged (44-year-old) TAs. Experimental data include 19 different biaxial loading protocols for each specimen.

Author Manuscript Author Manuscript Author Manuscript Author Manuscript

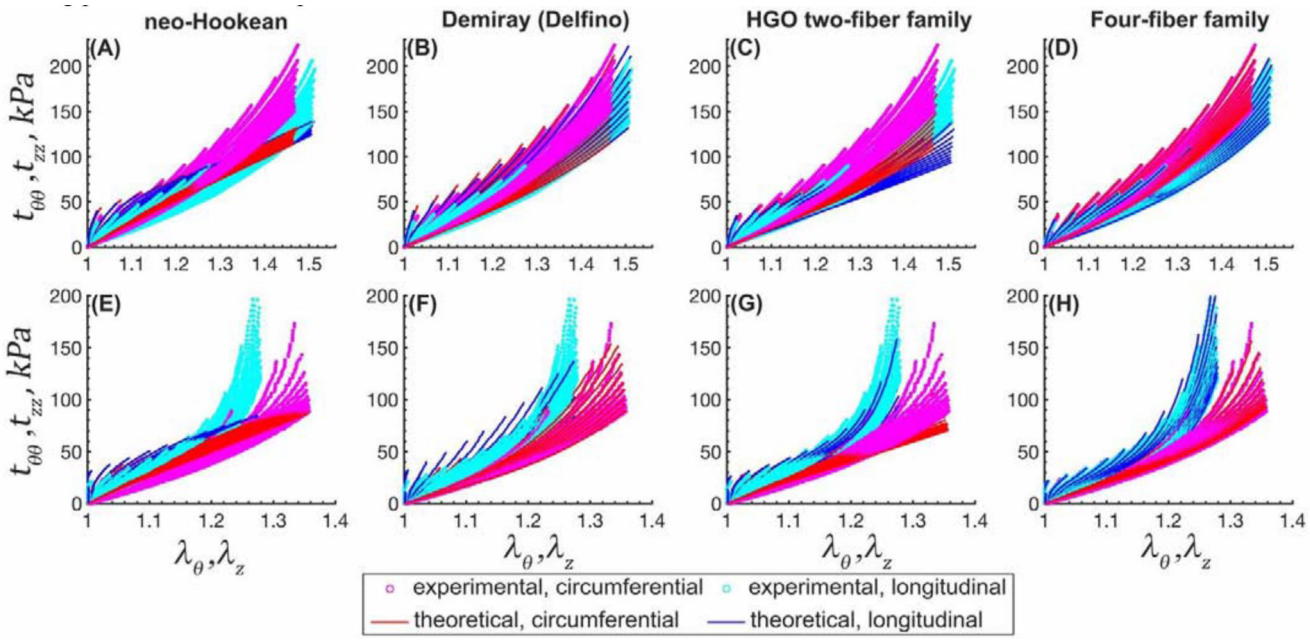

Figure 12:

Experimental stress-stretch data from 19 different biaxial loading protocols (cyan [longitudinal] and magenta [circumferential] dots) and model fits (solid blue [longitudinal] and red [circumferential] lines) for a 14 (top row) and 44 (bottom row) year-old TAs. (A,E) neo-Hookean, (B,F) Demiray (Delfino), (C,G) HGO two-fiber family, and (D,H) four-fiber family models. Please note that the stretch axes limits are different for the top and bottom plots.

6.5 Variability of aortic mechanical properties within age groups

The four-fiber family constitutive parameters representing the 25th and 75th percentiles within each age group are summarized in Table 4 and Table 5, respectively. Constitutive parameters for the softest and stiffest samples in each age group defined by the average stretch at 100 kPa biaxial stress, are reported in Table 6 and Table 7, respectively, along with risk factors in these subjects.

7 REFERENCES

[1]. Humphrey JD, Cardiovascular Solid Mechanics, Springer New York, New York, NY, 2002 10.1007/978-0-387-21576-1.

[2]. Gasser TC, Aorta, Biomech. Living Organs (2017) 169–191. 10.1016/B978-0-12-804009-6.00008-0.

[3]. García-Herrera CM, Celentano DJ, Cruchaga MA, Rojo FJ, Atienza M, V Guinea G, Goicolea JM, Atienza JM, Mechanical characterisation of the human thoracic descending aorta: experiments and modelling, Comput. Methods Biomech. Biomed. Engin 15 (2012) 185–193. 10.1080/10255842.2010.520704. [PubMed: 21480018]

[4]. Westerhof N, Lankhaar J-W, Westerhof BE, The arterial Windkessel, Med. Biol. Eng. Comput 47 (2009) 131–141. 10.1007/s11517-008-0359-2. [PubMed: 18543011]

[5]. Belz GG, Elastic properties and Windkessel function of the human aorta, Cardiovasc. Drugs Ther 9 (1995) 73–83. 10.1007/BF00877747. [PubMed: 7786838]

Author Manuscript Author Manuscript Author Manuscript Author Manuscript

[6]. Niestrawska JA, Viertler C, Regitnig P, Cohnert TU, Sommer G, Holzapfel GA, Microstructure and mechanics of healthy and aneurysmatic abdominal aortas: experimental analysis and modelling, J. R. Soc. Interface 13 (2016) 20160620 10.1098/rsif.2016.0620. [PubMed: 27903785]

[7]. O'Connell MK, Murthy S, Phan S, Xu C, Buchanan J, Spilker R, Dalman RL, Zarins CK, Denk W, Taylor CA, The three-dimensional micro- and nanostructure of the aortic medial lamellar unit measured using 3D confocal and electron microscopy imaging, Matrix Biol. 27 (2008) 171–181. 10.1016/J.MATBIO.2007.10.008. [PubMed: 18248974]

[8]. Humphrey JD, Eberth JF, Dye WW, Gleason RL, Fundamental role of axial stress in compensatory adaptations by arteries, J. Biomech 42 (2009) 1–8. 10.1016/j.jbiomech.2008.11.011.Fundamental. [PubMed: 19070860]

[9]. Mithieux SM, Weiss AS, Elastin., Adv. Protein Chem 70 (2005) 437–61. 10.1016/S0065-3233(05)70013-9. [PubMed: 15837523]

[10]. Wolinsky H, Glagov S, A Lamellar Unit of Aortic Medial Structure and Function in Mammals, 1967.

[11]. Wolinsky H, Glagov S, Structural Basis for the Static Mechanical Properties of the Aortic Media, 1963.

[12]. Clark JM, Glagov S, Transmural Organization of the Arterial Media The Lamellar Unit Revisited, 1984.

[13]. Wolinsky H, Glagov S, Comparison of Abdominal and Thoracic Aortic Medial Structure in Mammals, Circ. Res 25 (1969) 677–686. 10.1161/01.RES.25.6.677. [PubMed: 5364644]

[14]. Cocciolone AJ, Hawes JZ, Staiculescu MC, Johnson EO, Murshed M, Wagenseil JE, Elastin, arterial mechanics, and cardiovascular disease, Am. J. Physiol. Circ. Physiol 315 (2018) H189–H205. 10.1152/ajpheart.00087.2018.

[15]. V Kamenskiy A, Dzenis YA, Kazmi SAJ, Pemberton MA, Pipinos III, Phillips NY, Herber K, Woodford T, Bowen RE, Lomneth CS, MacTaggart JN, Biaxial mechanical properties of the human thoracic and abdominal aorta, common carotid, subclavian, renal and common iliac arteries., Biomech. Model. Mechanobiol 13 (2014) 1341–59. 10.1007/s10237-014-0576-6. [PubMed: 24710603]

[16]. Lee H-Y, Oh B-H, Aging and Arterial Stiffness, Circ. J 74 (2010) 2257–2262. 10.1253/circj.CJ-10-0910. [PubMed: 20962429]

[17]. Sun Z, Aging, arterial stiffness, and hypertension, Hypertension. 65 (2015) 252–256. 10.1161/HYPERTENSIONAHA.114.03617. [PubMed: 25368028]

[18]. van Prehn J, Vincken KLL, Sprinkhuizen SMM, Viergever MAA, van Keulen JWW, van Herwaarden JAA, Moll FLL, Bartels LWW, Aortic Pulsatile Distention in Young Healthy Volunteers is Asymmetric: Analysis with ECG-gated MRI, Eur. J. Vasc. Endovasc. Surg 37 (2009) 168–174. 10.1016/j.ejvs.2008.11.007. [PubMed: 19046649]

[19]. Mitchell GF, Arterial stiffness and hypertension, Hypertension. 64 (2014) 13–18. 10.1161/HYPERTENSIONAHA.114.00921. [PubMed: 24752432]

[20]. Humphrey JD, Harrison DG, Figueroa CA, Lacolley P, Laurent S, Central Artery stiffness in hypertension and aging a problem with cause and consequence, Circ. Res 118 (2016) 379–381. 10.1161/CIRCRESAHA.115.307722. [PubMed: 26846637]

[21]. Tzilalis VD, May J, White GH, Stephen MS, Harris JP, Severe hypertension following implantation of endovascular grafts into the thoracic aorta of young patients, J. Endovasc. Ther. An Off. J. Int. Soc. Endovasc. Spec 12 (2005) 142–143. 10.1583/04-1458L.1.

[22]. Russo C, Jin Z, Takei Y, Hasegawa T, Koshaka S, Palmieri V, Elkind MSV, Homma S, Sacco RL, Di Tullio MR, Arterial wave reflection and subclinical left ventricular systolic dysfunction, J. Hypertens 29 (2011) 574–582. 10.1097/HJH.0b013e328342ca56. [PubMed: 21169863]

[23]. Kadoglou NPE, Moulakakis KG, Papadakis I, Ikonomidis I, Alepaki M, Spathis A, Karakitsos P, Lekakis J, Liapis CD, Differential Effects of Stent-Graft Fabrics on Arterial Stiffness in Patients Undergoing Endovascular Aneurysm Repair, J. Endovasc. Ther 21 (2014) 850–858. 10.1583/14-4772MR.1. [PubMed: 25453890]

Author Manuscript Author Manuscript Author Manuscript Author Manuscript

[24]. Ioannou CV, Morel DR, Katsamouris AN, Katranitsa S, Startchik I, Kalangos A, Westerhof N, Stergiopulos N, Left ventricular hypertrophy induced by reduced aortic compliance, J. Vasc. Res 46 (2009) 417–425. 10.1159/000194272. [PubMed: 19155633]

[25]. Shirani J, Pick R, Roberts WC, Maron BJ, Morphology and significance of the left ventricular collagen network in young patients with hypertrophic cardiomyopathy and sudden cardiac death, J. Am. Coll. Cardiol 35 (2000) 36–44. 10.1016/S0735-1097(99)00492-1. [PubMed: 10636256]

[26]. Gates PE, Tanaka H, Graves J, Seals DR, Left ventricular structure and diastolic function with human ageing. Relation to habitual exercise and arterial stiffness, Eur. Heart J 24 (2003) 2213–2220. 10.1016/j.ehj.2003.09.026. [PubMed: 14659773]

[27]. Redfield MM, Jacobsen SJ, Borlaug BA, Rodeheffer RJ, Kass DA, Age- and gender-related ventricular-vascular stiffening: A community-based study, Circulation. 112 (2005) 2254–2262. 10.1161/CIRCULATIONAHA.105.541078. [PubMed: 16203909]

[28]. Lattouf R, Younes R, Lutomski D, Naaman N, Godeau G, Senni K, Changotade S, Picrosirius Red Staining: A Useful Tool to Appraise Collagen Networks in Normal and Pathological Tissues, J. Histochem. Cytochem 62 (2014) 751–758. 10.1369/0022155414545787. [PubMed: 25023614]

[29]. Shirwany NA, Zou M, Arterial stiffness: a brief review, Acta Pharmacol. Sin 31 (2010) 1267–1276. 10.1038/aps.2010.123. [PubMed: 20802505]

[30]. Zieman SJ, Melenovsky V, Kass DA, Mechanisms, pathophysiology, and therapy of arterial stiffness., Arterioscler. Thromb. Vasc. Biol 25 (2005) 932–43. 10.1161/01.ATV.0000160548.78317.29. [PubMed: 15731494]

[31]. Quinaglia T, Bensalah MZ, Bollache E, Kachenoura N, Soulat G, Boutouyrie P, Laurent S, Mousseaux E, Differential impact of local and regional aortic stiffness on left ventricular remodeling, J. Hypertens 36 (2018) 1 10.1097/HJH.0000000000001597. [PubMed: 29076922]

[32]. Ohyama Y, Ambale-Venkatesh B, Noda C, Chugh AR, Teixido-Tura G, Kim JY, Donekal S, Yoneyama K, Gjesdal O, Redheuil A, Liu CY, Nakamura T, Wu CO, Hundley WG, Bluemke DA, Lima JAC, Association of aortic stiffness with left ventricular remodeling and reduced left ventricular function measured by magnetic resonance imaging: The multi-ethnic study of atherosclerosis, Circ. Cardiovasc. Imaging 9 (2016). 10.1161/CIRCIMAGING.115.004426.

[33]. Ohtsuka S, Kakihana M, Watanabe H, Sugishita Y, Chronically decreased aortic distensibility causes deterioration of coronary perfusion during increased left ventricular contraction, J. Am. Coll. Cardiol 24 (1994) 1406–1414. 10.1016/0735-1097(94)90127-9. [PubMed: 7930267]

[34]. O'Rourke MF, Safar ME, Relationship between aortic stiffening and microvascular disease in brain and kidney: Cause and logic of therapy, Hypertension. 46 (2005) 200–204. 10.1161/01.HYP.0000168052.00426.65. [PubMed: 15911742]

[35]. Mitchell GF, Van Buchem MA, Sigurdsson S, Gotal JD, Jonsdottir MK, Kjartansson Ó, Garcia M, Aspelund T, Harris TB, Gudnason V, Launer LJ, Arterial stiffness, pressure and flow pulsatility and brain structure and function: The Age, Gene/Environment Susceptibility-Reykjavik Study, Brain. 134 (2011) 3398–3407. 10.1093/brain/awr253. [PubMed: 22075523]

[36]. Safar ME, London GM, Plante GE, Arterial Stiffness and Kidney Function, Hypertension. 43 (2004) 163–168. 10.1161/01.HYP.0000114571.75762.b0. [PubMed: 14732732]

[37]. Hu JJ, Fossum TW, Miller MW, Xu H, Liu JC, Humphrey JD, Biomechanics of the porcine basilar artery in hypertension, Ann. Biomed. Eng 35 (2007) 19–29. 10.1007/s10439-006-9186-5. [PubMed: 17066325]

[38]. Iversen BM, Ofstad J, The effect of hypertension on glomerular structures and capillary permeability in passive Heymann glomerulonephritis, Microvasc. Res 34 (1987) 137–151. 10.1016/0026-2862(87)90049-5. [PubMed: 3670111]

[39]. Cooper LL, Rong J, Benjamin EJ, Larson MG, Levy D, Vita JA, Hamburg NM, Vasan RS, Mitchell GF, Components of hemodynamic load and cardiovascular events the framingham heart study, Circulation. 131 (2015) 354–361. 10.1161/CIRCULATIONAHA.114.011357. [PubMed: 25416177]

[40]. Maillard P, Mitchell GF, Himali JJ, Beiser A, Tsao CW, Pase MP, Satizabal CL, Vasan RS, Seshadri S, De Carli C, Effects of arterial stiffness on brain integrity in young adults from the framingham heart study, Stroke. 47 (2016) 1030–1036. 10.1161/STROKEAHA.116.012949. [PubMed: 26965846]

Author Manuscript Author Manuscript Author Manuscript Author Manuscript

[41]. Mitchell GF, Effects of central arterial aging on the structure and function of the peripheral vasculature: implications for end-organ damage, J. Appl. Physiol 105 (2008) 1652–1660. 10.1152/japplphysiol.90549.2008. [PubMed: 18772322]

[42]. Verhave JC, Fesler P, Du Cailar G, Ribstein J, Safar ME, Mimran A, Elevated pulse pressure is associated with low renal function in elderly patients with isolated systolic hypertension, Hypertension. 45 (2005) 586–591. 10.1161/01.HYP.0000158843.60830.cf. [PubMed: 15738348]

[43]. Safar ME, Plante GE, Mimran A, Arterial stiffness, pulse pressure, and the kidney, Am. J. Hypertens 28 (2015) 561–569. 10.1093/ajh/hpu206. [PubMed: 25480804]

[44]. Hashimoto J, Ito S, Central pulse pressure and aortic stiffness determine renal hemodynamics: Pathophysiological implication for microalbuminuria in hypertension, Hypertension. 58 (2011) 839–846. 10.1161/HYPERTENSIONAHA.111.177469. [PubMed: 21968753]

[45]. Bruno RM, Cartoni G, Stea F, Armenia S, Bianchini E, Buralli S, Giannarelli C, Taddei S, Ghiadoni L, Carotid and aortic stiffness in essential hypertension and their relation with target organ damage, J. Hypertens 35 (2017) 310–318. 10.1097/HJH.0000000000001167. [PubMed: 27841779]

[46]. Elias MF, Torres RV, Davey A, Parameters of Left Ventricular Mass and Dementia: Moving the Literature Forward, Hypertension. 71 (2018) 411–412. 10.1093/ageing/afw169.8. [PubMed: 29378855]

[47]. Rabin J, Harris DG, Crews GA, Ho M, Taylor BS, Sarkar R, O'Connor JV, Scalea TM, Crawford RS, Early aortic repair worsens concurrent traumatic brain injury, Ann. Thorac. Surg 98 (2014) 46–52. 10.1016/j.athoracsur.2014.04.025. [PubMed: 24857854]

[48]. Vaishnav RN, Vossoughi J, ESTIMATION OF RESIDUAL STRAINS IN AORTIC SEGMENTS, in: Biomed. Eng. II, Elsevier, 1983: pp. 330–333. 10.1016/B978-0-08-030145-7.50078-7.

[49]. Chuong CJ, Fung YC, Residual Stress in Arteries, in: Front. Biomech, Springer New York, New York, NY, 1986: pp. 117–129. 10.1007/978-1-4612-4866-8_9.

[50]. Rachev A, Greenwald S, Residual strains in conduit arteries, J. Biomech 36 (2003) 661–670. 10.1016/S0021-9290(02)00444-X. [PubMed: 12694996]

[51]. Horný L, Netušil M, Voňavková T, Axial prestretch and circumferential distensibility in biomechanics of abdominal aorta., Biomech. Model. Mechanobiol 13 (2013) 783–799. 10.1007/s10237-013-0534-8. [PubMed: 24136338]

[52]. Horny L, Adamek T, Gultova E, Zitny R, Vesely J, Chlup H, Konvickova S, Correlations between age, prestrain, diameter and atherosclerosis in the male abdominal aorta., J. Mech. Behav. Biomed. Mater 4 (2011) 2128–32. 10.1016/j.jmbbm.2011.07.011. [PubMed: 22098912]

[53]. Horný L, Adámek T, Kulvajtová M, A comparison of age-related changes in axial prestretch in human carotid arteries and in human abdominal aorta., Biomech. Model. Mechanobiol (2016). 10.1007/s10237-016-0797-y.

[54]. Cheng D, Martin J, Shennib H, Dunning J, Muneretto C, Schueler S, Von Segesser L, Segeant P, Turina Marko, Endovascular Aortic Repair Versus Open Surgical Repair for Descending Thoracic Aortic Disease A Systematic Review and Meta-Analysis of Comparative Studies, J. Am. Coll. Cardiol 55 (2010) 986–1001. [PubMed: 20137879]

[55]. Xenos ES, Abedi NN, Davenport DL, Minion DJ, Hamdallah O, Sorial EE, Endean ED, SERIAL EE, Meta-analysis of endovascular vs open repair for traumatic descending thoracic aortic rupture., J. Vasc. Surg 48 (2008) 1343–51. 10.1016/j.jvs.2008.04.060. [PubMed: 18632242]

[56]. Reuben BC, Whitten MG, Sarfati M, Kraiss LW, Increasing use of endovascular therapy in acute arterial injuries: analysis of the National Trauma Data Bank., J. Vasc. Surg 46 (2007) 1222–1226. 10.1016/j.jvs.2007.08.023. [PubMed: 18154998]

[57]. Kamenskiy A, Seas A, Deegan P, Poulson W, Anttila E, Sim S, Desyatova A, MacTaggart J, Constitutive description of human femoropopliteal artery aging, Biomech. Model. Mechanobiol 16 (2017) 681–692. 10.1007/s10237-016-0845-7. [PubMed: 27771811]

[58]. Jadidi M, Desyatova A, MacTaggart J, Kamenskiy A, Mechanical stresses associated with flattening of human femoropopliteal artery specimens during planar biaxial testing and their effects on the calculated physiologic stress-stretch state., Biomech. Model. Mechanobiol 18 (2019) 1591–1605. 10.1007/s10237-019-01162-0. [PubMed: 31069592]

Author Manuscript Author Manuscript Author Manuscript Author Manuscript

[59]. Holzapfel G. a., Ogden RW, Constitutive modelling of arteries, Proc. R. Soc. A Math. Phys. Eng. Sci 466 (2010) 1551–1597. 10.1098/rspa.2010.0058.

[60]. Martins PALS, Natal Jorge RM, Ferreira AJM, A Comparative Study of Several Material Models for Prediction of Hyperelastic Properties: Application to Silicone-Rubber and Soft Tissues, Strain. 42 (2006) 135–147. 10.1111/j.1475-1305.2006.00257.x.

[61]. Delfino A, Analysis of stress field in a model of the human carotid bifurcation, Ecole Polytechnique Federale DeLausanne, 1996 10.5075/epfl-thesis-1599.

[62]. Demiray H, Weizsacker HW, Pascale K, Erbay HA, A Stress-Strain Relation for a Rat Abdominal Aorta, J Biomech. 21 (1988) 369–374. [PubMed: 3417689]

[63]. Holzapfel GA, Gasser TC, Ogden RW, W OR, A New Constitutive Framework For Arterial Wall Mechanics And A Comparative Study of Material Models, J Elast. 61 (2000) 1–48.

[64]. Ferruzzi J, Vorp DA, Humphrey JD, On constitutive descriptors of the biaxial mechanical behaviour of human abdominal aorta and aneurysms., J R Soc Interface. 8 (2011) 435–450. [PubMed: 20659928]

[65]. Anttila E, Balzani D, Desyatova A, Deegan P, MacTaggart J, Kamenskiy A, Mechanical Damage Characterization in Human Femoropopliteal Arteries of Different Ages, Acta Biomater. (2019) Accepted.

[66]. Desyatova A, MacTaggart J, Kamenskiy A, Constitutive modeling of human femoropopliteal artery biaxial stiffening due to aging and diabetes., Acta Biomater. 64 (2017) 50–58. 10.1016/j.actbio.2017.09.042. [PubMed: 28974476]

[67]. V Kamenskiy A, Pipinos II, Dzenis YA, Phillips NY, Desyatova AS, Kitson J, Bowen R, MacTaggart JN, Effects of age on the physiological and mechanical characteristics of human femoropopliteal arteries., Acta Biomater. 11 (2015) 304–13. 10.1016/j.actbio.2014.09.050. [PubMed: 25301303]

[68]. Desyatova A, MacTaggart J, Poulson W, Deegan P, Lomneth C, Sandip A, Kamenskiy A, The choice of a constitutive formulation for modeling limb flexion-induced deformations and stresses in the human femoropopliteal arteries of different ages, Biomech. Model. Mechanobiol 16 (2017) 775–785. 10.1007/s10237-016-0852-8. [PubMed: 27868162]

[69]. Baek S, Gleason RL, Rajagopal KR, Humphrey JD, Theory of small on large: Potential utility in computations of fluid–solid interactions in arteries, Comput. Methods Appl. Mech. Eng 196 (2007) 3070–3078. 10.1016/j.cma.2006.06.018.

[70]. Zeinali-Davarani S, Choi J, Baek S, On parameter estimation for biaxial mechanical behavior of arteries, J. Biomech 42 (2009) 524–530. 10.1016/J.JBIOMECH.2008.11.022. [PubMed: 19159887]

[71]. Sommer G, a Holzapfel G, 3D constitutive modeling of the biaxial mechanical response of intact and layer-dissected human carotid arteries., J. Mech. Behav. Biomed. Mater 5 (2012) 116–28. 10.1016/j.jmbbm.2011.08.013. [PubMed: 22100086]

[72]. Han HC, Fung YC, Longitudinal strain of canine and porcine aortas, J. Biomech 28 (1995) 637–641. 10.1016/0021-9290(94)00091-H. [PubMed: 7775500]

[73]. Fehervary H, Smoljkić M, Vander Sloten J, Famaey N, Planar biaxial testing of soft biological tissue using rakes: A critical analysis of protocol and fitting process, J. Mech. Behav. Biomed. Mater 61 (2016) 135–151. 10.1016/j.jmbbm.2016.01.011. [PubMed: 26854936]

[74]. Stålhand J, Klarbring a, Aorta in vivo parameter identification using an axial force constraint., Biomech. Model. Mechanobiol 3 (2005) 191–9. 10.1007/s10237-004-0057-4. [PubMed: 15776254]

[75]. Weizsacker H, Lambert H, Pascale K, Analysis of the passive mechanical properties of rat carotid arteries, J. Biomech (1983).

[76]. Tsamis A, Phillippi JA, Koch RG, Pasta S, D'Amore A, Watkins SC, Wagner WR, Gleason TG, Vorp DA, Fiber micro-architecture in the longitudinal-radial and circumferential-radial planes of ascending thoracic aortic aneurysm media, J. Biomech 46 (2013) 2787–2794. 10.1016/j.jbiomech.2013.09.003. [PubMed: 24075403]

[77]. Deplano V, Boufi M, Gariboldi V, Loundou AD, D'Journo XB, Cautela J, Djemli A, Alimi YS, Mechanical characterisation of human ascending aorta dissection, J. Biomech 94 (2019) 138–146. 10.1016/j.jbiomech.2019.07.028. [PubMed: 31400813]

Author Manuscript Author Manuscript Author Manuscript Author Manuscript

[78]. Tsamis A, Krawiec JT, a Vorp D, Elastin and collagen fibre microstructure of the human aorta in ageing and disease: a review., J. R. Soc. Interface 10 (2013) 20121004 10.1098/rsif.2012.1004. [PubMed: 23536538]

[79]. Humphrey JD, Dufresne ER, Schwartz M. a., Mechanotransduction and extracellular matrix homeostasis, Nat. Rev. Mol. Cell Biol 15 (2014) 802–812. 10.1038/nrm3896. [PubMed: 25355505]

[80]. Humphrey JD, Vascular adaptation and mechanical homeostasis at tissue, cellular, and sub-cellular levels., Cell Biochem. Biophys 50 (2008) 53–78. 10.1007/s12013-007-9002-3. [PubMed: 18209957]

[81]. Vande-Geest JP, Sacks MS, Vorp DA, Age dependency of the biaxial biomechanical behavior of human abdominal aorta., J Biomech Eng. 126 (2004) 815–822. [PubMed: 15796340]

[82]. Roccabianca S, Figueroa CA, Tellides G, Humphrey JD, Quantification of regional differences in aortic stiffness in the aging human, J. Mech. Behav. Biomed. Mater 29 (2014) 618–634. 10.1016/j.jmbbm.2013.01.026. [PubMed: 23499251]

[83]. Izzo JL, Arterial stiffness and the systolic hypertension syndrome, Curr. Opin. Cardiol 19 (2004) 341–352. 10.1097/01.hco.0000126581.89648.10. [PubMed: 15218394]

[84]. Kamenskiy AV, Pipinos II, Carson JS, MacTaggart JN, Baxter BT, Age and disease-related geometric and structural remodeling of the carotid artery, J. Vasc. Surg 62 (2015) 1521–1528. 10.1016/J.JVS.2014.10.041. [PubMed: 25499709]

[85]. Cavalcante JL, Lima JAC, Redheuil A, Al-Mallah MH, Aortic Stiffness: Current Understanding and Future Directions, J. Am. Coll. Cardiol 57 (2011) 1511–1522. 10.1016/J.JACC.2010.12.017. [PubMed: 21453829]

[86]. Weisbecker H, Viertler C, Pierce DM, Holzapfel GA, The role of elastin and collagen in the softening behavior of the human thoracic aortic media, J. Biomech 46 (2013) 1859–1865. 10.1016/j.jbiomech.2013.04.025. [PubMed: 23735660]

[87]. Silacci paolo, Advanced glycation end-products as a potential target for treatment of cardiovascular disease, J. Hypertens 20 (2002) 1483–1485. [PubMed: 12172306]

[88]. Yim MB, Yim H-S, Lee C, Kang S-O, Chock PB, Protein Glycation, Ann. N. Y. Acad. Sci 928 (2006) 48–53. 10.1111/j.1749-6632.2001.tb05634.x.

[89]. Oomen PJA, Loerakker S, van Geemen D, Neggers J, Goumans M-JTH, van den Bogaerdt AJ, Bogers AJJC, Bouten CVC, Baaijens FPT, Age-dependent changes of stress and strain in the human heart valve and their relation with collagen remodeling, Acta Biomater. 29 (2016) 161–169. 10.1016/J.ACTBIO.2015.10.044. [PubMed: 26537200]

[90]. Sell DR, Monnier VM, Molecular basis of arterial stiffening: role of glycation - a mini-review., Gerontology. 58 (2012) 227–37. 10.1159/000334668. [PubMed: 22222677]

[91]. Peña JA, Martínez MA, Peña E, Layer-specific residual deformations and uniaxial and biaxial mechanical properties of thoracic porcine aorta, J. Mech. Behav. Biomed. Mater 50 (2015) 55–69. 10.1016/j.jmbbm.2015.05.024. [PubMed: 26103440]

[92]. Holzapfel GA, Ogden RW, Modelling the layer-specific three-dimensional residual stresses in arteries, with an application to the human aorta, J. R. Soc. Interface 7 (2010) 787–799. [PubMed: 19828496]

[93]. Hartley MC, Langan EM, Cull DL, Taylor SM, Carsten CG, Blackhurst DW, Evaluation of the diameter of the proximal descending thoracic aorta with age: implications for thoracic aortic stent grafting., Ann. Vasc. Surg 23 (2009) 639–44. 10.1016/j.avsg.2009.05.001. [PubMed: 19616402]

[94]. Kamenskiy A, Miserlis D, Adamson P, Adamson M, Knowles T, Neme J, Koutakis P, Phillips N, Pipinos I, MacTaggart J, Patient demographics and cardiovascular risk factors differentially influence geometric remodeling of the aorta compared with the peripheral arteries., Surgery. 158 (2015) PubMed PMID 26096560; NIHMSID: NIHMS697336. 10.1016/j.surg.2015.05.013.

[95]. Hickson SS, Butlin M, Graves M, Taviani V, Avolio AP, McEniery CM, Wilkinson IB, The Relationship of Age With Regional Aortic Stiffness and Diameter, JACC Cardiovasc. Imaging 3 (2010) 1247–1255. 10.1016/J.JCMG.2010.09.016. [PubMed: 21163453]

[96]. Sokolis DP, Savva GD, Papadodima SA, Kourkoulis SK, Regional distribution of circumferential residual strains in the human aorta according to age and gender, J. Mech. Behav. Biomed. Mater 67 (2017) 87–100. 10.1016/j.jmbbm.2016.12.003. [PubMed: 27988442]

Author Manuscript Author Manuscript Author Manuscript Author Manuscript

[97]. Holzapfel GA, Sommer G, Auer M, Regitnig P, Ogden RW, Layer-specific 3D residual deformations of human aortas with non-atherosclerotic intimal thickening., Ann Biomed Eng. 35 (2007) 530–545. [PubMed: 17285364]

[98]. Humphrey JD, Possible mechanical roles of glycosaminoglycans in thoracic aortic dissection and associations with dysregulated transforming growth factor-β, J. Vasc. Res 50 (2012) 1–10. 10.1159/000342436. [PubMed: 23018968]

[99]. Draney CA, Xu M, Zarins C, Taylor CK, Circumferentially Nonuniform Wall Thickness and Lamellar Structure Correlates With Cyclic Strain in the Porcine Descending Thoracic Aorta, Summer Bioeng. Conf June 25–29 (2003).

[100]. Dridi SM, Foucault Bertaud A, Tchen SI, Senni K, Ejeil AL, Pellat B, Lyonnet S, Bonnet D, Charpiot P, Godeau G, Vascular Wall Remodeling in Patients with Supravalvular Aortic Stenosis and Williams Beuren Syndrome, J Vasc Res. 42 (2005) 190–201. 10.1159/000085141. [PubMed: 15832055]

[101]. Halloran BG, Davis VA, McManus BM, Lynch TG, Baxter BT, Localization of Aortic Disease Is Associated with Intrinsic Differences in Aortic Structure, J. Surg. Res 59 (1995) 17–22. 10.1006/JSRE.1995.1126. [PubMed: 7630123]

[102]. Morrison TM, Choi G, Zarins CK, Taylor CA, Circumferential and longitudinal cyclic strain of the human thoracic aorta: age-related changes., J Vasc Surg. 49 (2009) 1029–1036. [PubMed: 19341890]

[103]. Martufi G, Gasser TC, Turnover of fibrillar collagen in soft biological tissue with application to the expansion of abdominal aortic aneurysms, J. R. Soc. Interface (2012). 10.1098/rsif.2012.0416.

[104]. Holzapfel GA, Gasser TC, Computational stress-deformation analysis of arterial walls including high-pressure response, Int. J. Cardiol 116 (2007) 78–85. 10.1016/j.ijcard.2006.03.033. [PubMed: 16822562]

[105]. Chaudhry HR, Bukiet B, Davis A, Ritterj AB, Residual Stresses in Oscillating Thoracic Arteries Reduce Circumferential Stresses and Stress Gradients, 30 (1997) 57–62.

[106]. Amabili M, Balasubramanian P, Bozzo I, Breslavsky ID, Ferrari G, Layer-specific hyperelastic and viscoelastic characterization of human descending thoracic aortas, J. Mech. Behav. Biomed. Mater 99 (2019) 27–46. 10.1016/j.jmbbm.2019.07.008. [PubMed: 31330442]

[107]. Holzapfel GA, Schriefl AJ, Wolinski H, Regitnig P, Kohlwein SD, An automated approach for three-dimensional quantification of fibrillar structures in optically cleared soft biological tissues, J. R. Soc. Interface (2012). 10.1098/rsif.2012.0760.

[108]. König K, Schenke-Layland K, Riemann I, Stock UA, Multiphoton autofluorescence imaging of intratissue elastic fibers, Biomaterials. 26 (2005) 495–500. 10.1016/J.BIOMATERIALS.2004.02.059. [PubMed: 15276357]

[109]. Hemmasizadeh A, Tsamis A, Cheheltani R, Assari S, D'Amore A, Autieri M, Kiani MF, Pleshko N, Wagner WR, Watkins SC, Vorp D, Darvish K, Correlations between transmural mechanical and morphological properties in porcine thoracic descending aorta, J. Mech. Behav. Biomed. Mater 47 (2015) 12–20. 10.1016/J.JMBBM.2015.03.004. [PubMed: 25837340]

[110]. Ferruzzi J, Di Achille P, Tellides G, Humphrey JD, Combining in vivo and in vitro biomechanical data reveals key roles of perivascular tethering in central artery function, PLoS One. 13 (2018) 1–21. 10.1371/journal.pone.0201379.

[111]. Berenson GS, Srinivasan SR, Bao W, Newman WP, Tracy RE, Wattigney WA, Association between multiple cardiovascular risk factors and atherosclerosis in children and young adults. The Bogalusa Heart Study., N. Engl. J. Med 338 (1998) 1650–6. 10.1056/NEJM199806043382302. [PubMed: 9614255]

Author Manuscript Author Manuscript Author Manuscript Author Manuscript

Statement of significance

This manuscript describes mechanical and structural changes occurring in human thoracic aortas with age, and presents material parameters for 4 commonly used constitutive models. Presented data can help better understand aortic pathology, inform the development of animal models that simulate human aging, and assist with designing devices for open and endovascular aortic repairs.

Author Manuscript Author Manuscript Author Manuscript Author Manuscript

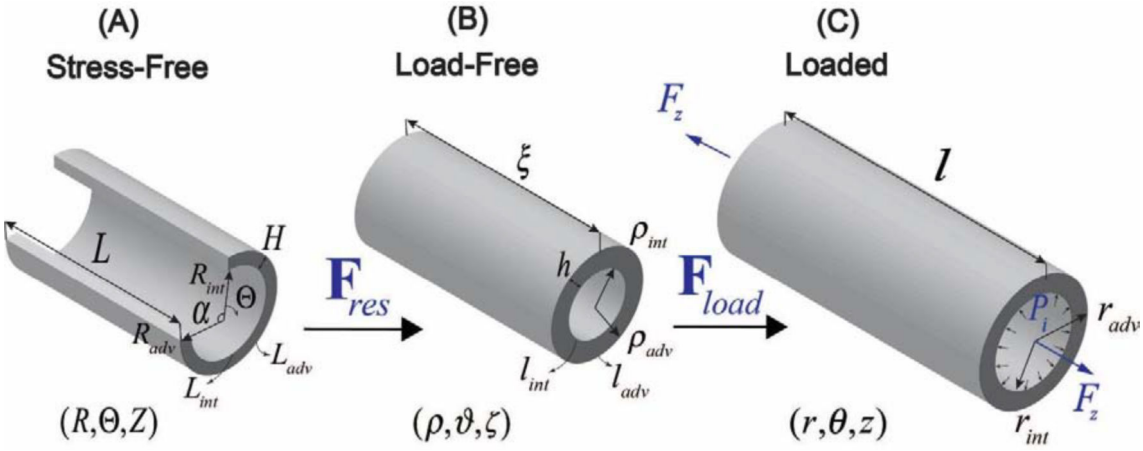

Figure 1:

Kinematics of the TA demonstrating (A) *stress-free* configuration obtained by radially opening the aorta, (B) *load-free* configuration with no internal pressure or longitudinal pre-stretch, and (C) the *in vivo loaded* state.

Author Manuscript Author Manuscript Author Manuscript Author Manuscript

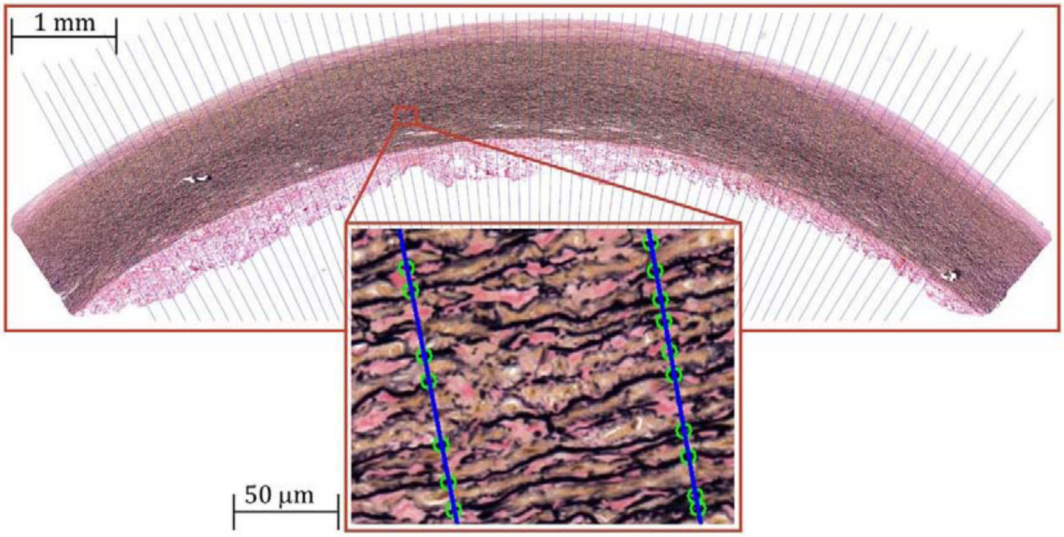

Figure 2:

A representative Verhoeff-Van Gieson (VVG)-stained longitudinal section of a 39-year-old TA demonstrating the algorithm of counting the elastic lamellae along the length of the blue lines drawn across the tunica media. Green circles on the lines illustrate the elastic lamellae that are counted along each line. Note that interlamellar fibers were not counted. Verhoeff-Van Gieson (VVG) stain: elastin is black, collagen is red, smooth muscle is brown.

Author Manuscript Author Manuscript Author Manuscript Author Manuscript

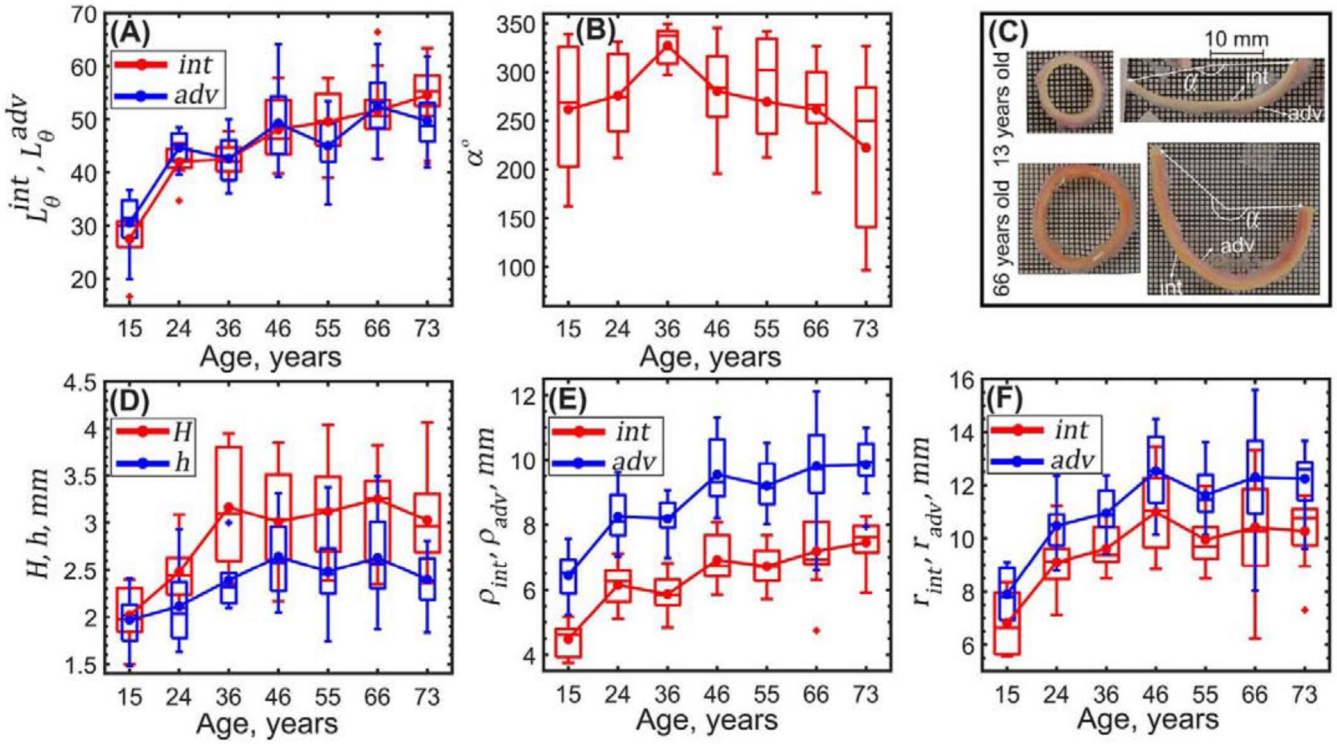

Figure 3:

Changes wth age in (A) *stress-free* radially-cut aortic ring lengths measured on the intimal L_θ^{int} (red) and adventitial L_θ^{adv} (blue) surfaces and (B) circumferential opening angle. (C) Radially-cut ring curves intima (int) inward in young TAs while in old TAs it curves adventitia (adv) inward. (D) Changes in *stress-free H* (red) and *load-free h* (blue) aortic wall thicknesses, (E) *load-free* radii ρ_{int}, ρ_{adv} and (F) calculated *loaded* aortic radii r_{int}, r_{adv} on the intimal (red) and adventitial (blue) surfaces. Here boxes bound 25th and 75th percentiles for each age group, median and average values are marked with a line and a dot within each box, whiskers extend to the 5th and 95th percentiles, and the outliers are displayed with a + sign.

Author Manuscript Author Manuscript Author Manuscript Author Manuscript

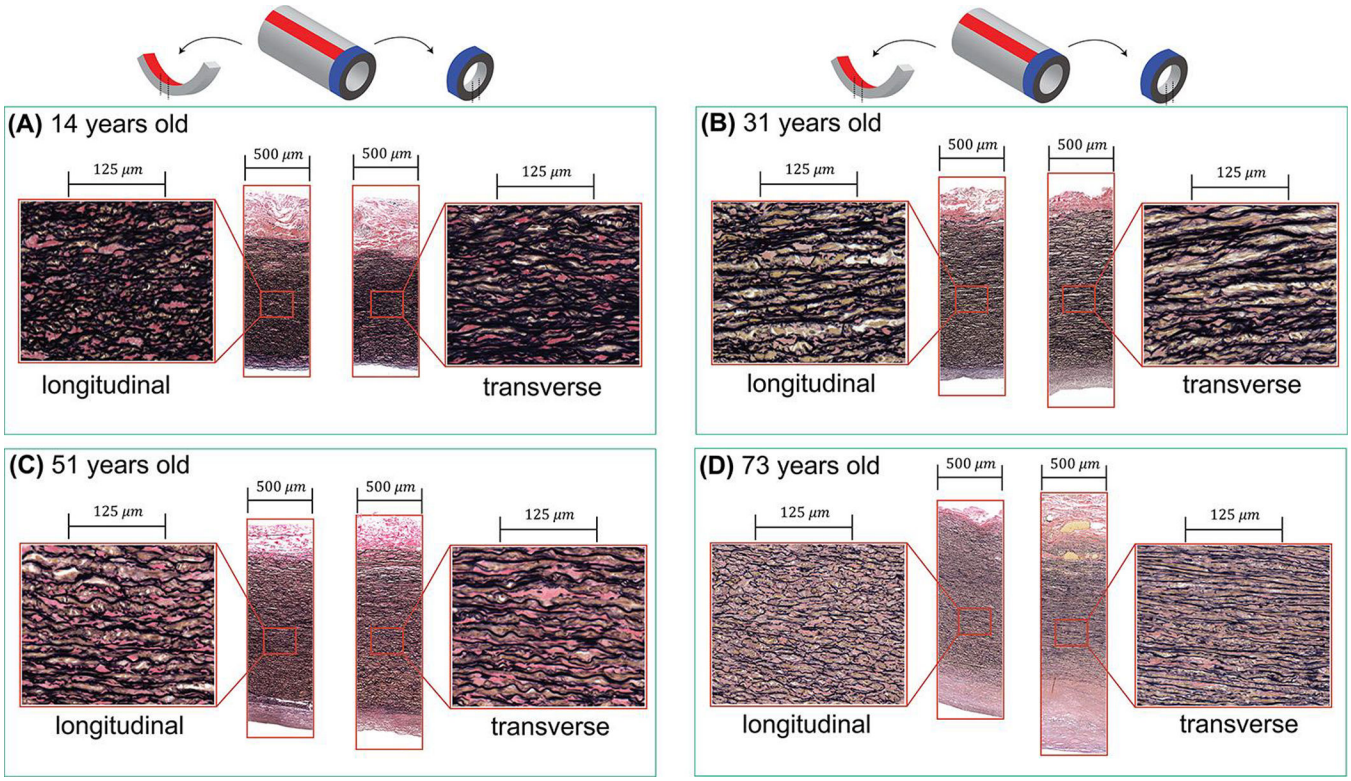

Figure 4:

Representative histological images of the longitudinal (left panels) and transverse (right panels) sections of four TA specimens from different age groups. Aortas are from (A) 14-year-old, (B) 31-year-old, (C) 51-year-old and (D) 73-year-old subjects. In young TA samples, the elastic lamellae are thick, undulated, and are located close to each other, while the opposite is observed for old TAs. Verhoeff-Van Gieson (VVG) stain: elastin is black, collagen is red, smooth muscle is brown.

Author Manuscript Author Manuscript Author Manuscript Author Manuscript

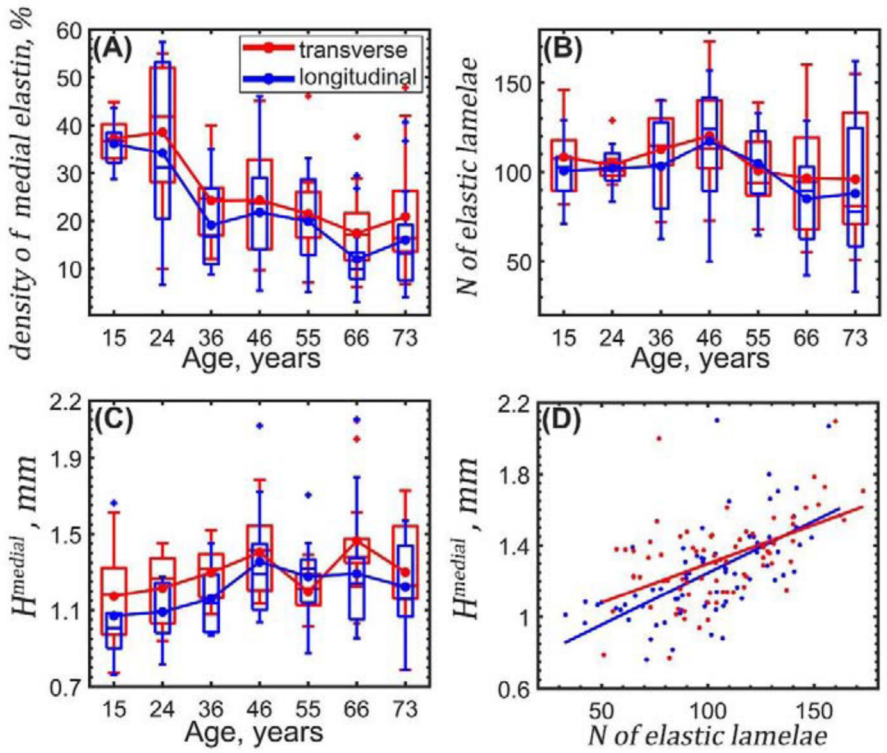

Figure 5:

Changes with age in elastin content evaluated using transverse (red) and longitudinal (blue) aortic sections. (A) density of elastin in the medial layer, (B) number of elastic lamellae in the medial layer, (C) thickness of the tunica media H^{medial}, and (D) thickness of tunica media as a function of the number of elastic lamellae. Here boxes bound 25th and 75th percentiles for each age group, median and average values are marked with a vertical line and a dot within each box, whiskers extend to the 5th and 95th percentiles, and the outliers are displayed with a + sign.

Author Manuscript Author Manuscript Author Manuscript Author Manuscript

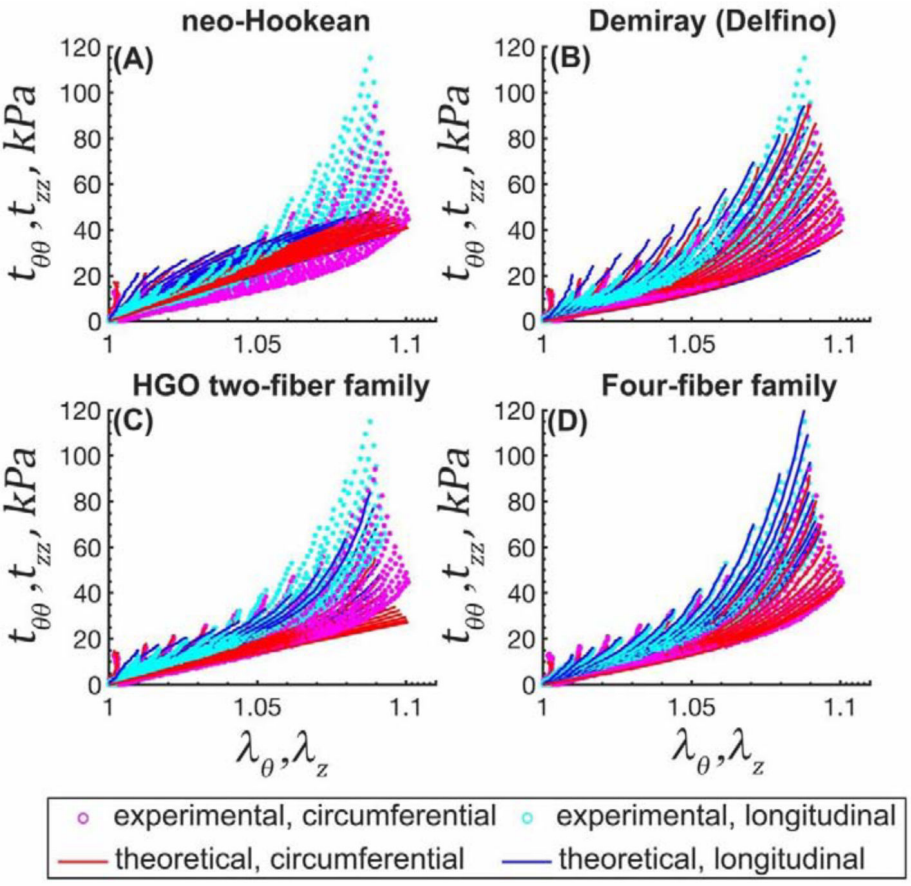

Figure 6:

Experimental stress-stretch data from 19 different biaxial loading protocols (cyan [longitudinal] and magenta [circumferential] dots) and model fits (solid blue [longitudinal] and red [circumferential] lines) for a 72 years old TA. (A) neo-Hookean, (B) Demiray (Delfino), (C) HGO two-fiber family, and (D) four-fiber family models.

Author Manuscript Author Manuscript Author Manuscript Author Manuscript

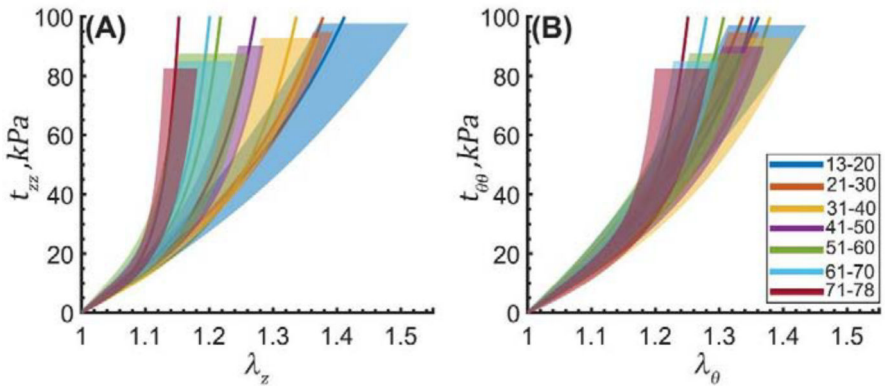

Figure 7:

Average equibiaxial stress-stretch curves for the TAs in 7 age groups plotted in the (A) longitudinal and (B) circumferential directions. Legend summarizes age range in each group (years). Variability within each age group is demonstrated by the shaded semi-transparent regions that bound 25th and 75th percentile ranges. They have different heights for better visual representation.

Author Manuscript Author Manuscript Author Manuscript Author Manuscript

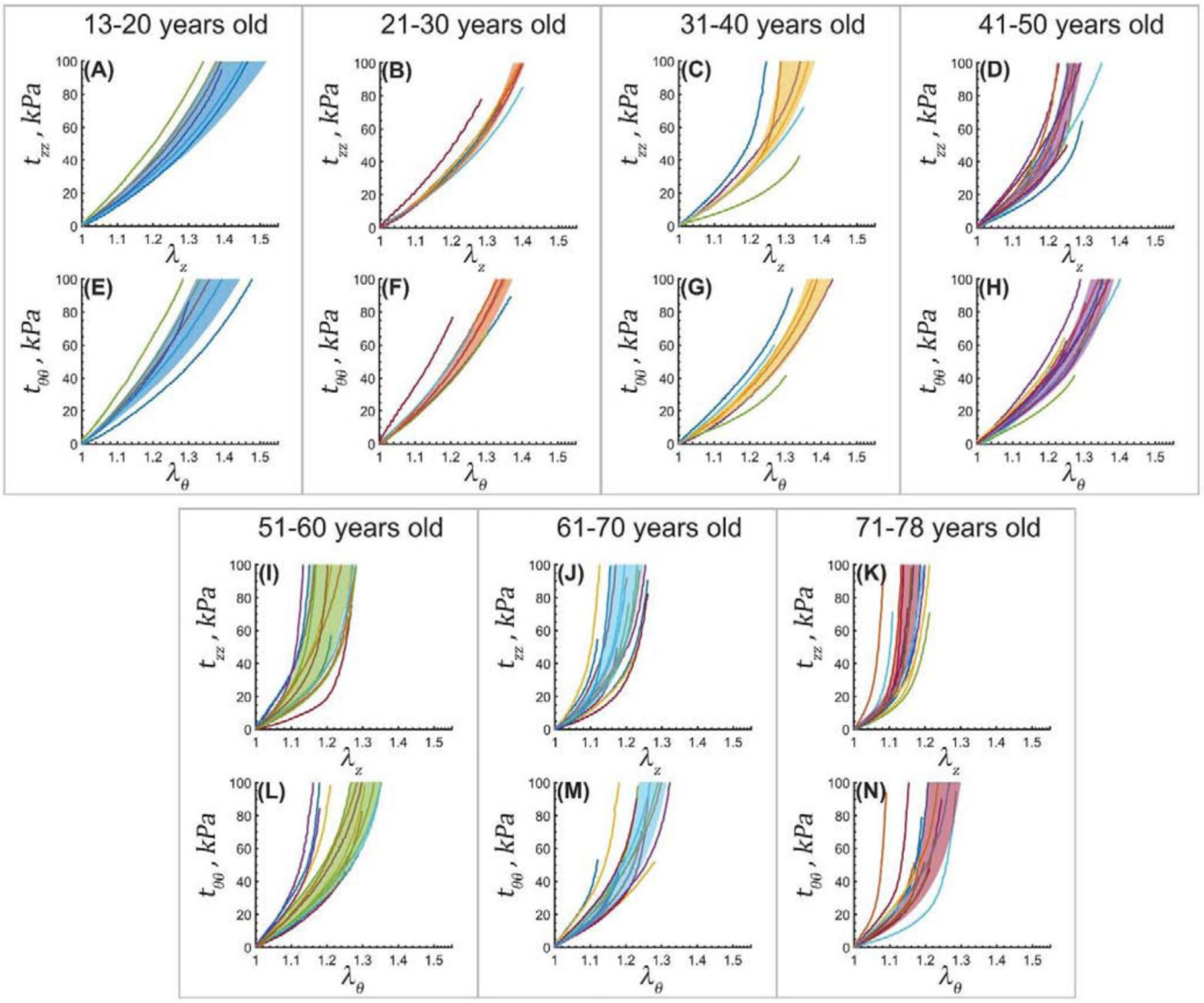

Figure 8:

Experimental equibiaxial stress-stretch responses in the longitudinal (z) and circumferential (θ) directions for aortas in 7 age groups. Variability within each age group is demonstrated by the shaded semi-transparent regions that bound 25th and 75th percentile ranges.

Author Manuscript Author Manuscript Author Manuscript Author Manuscript

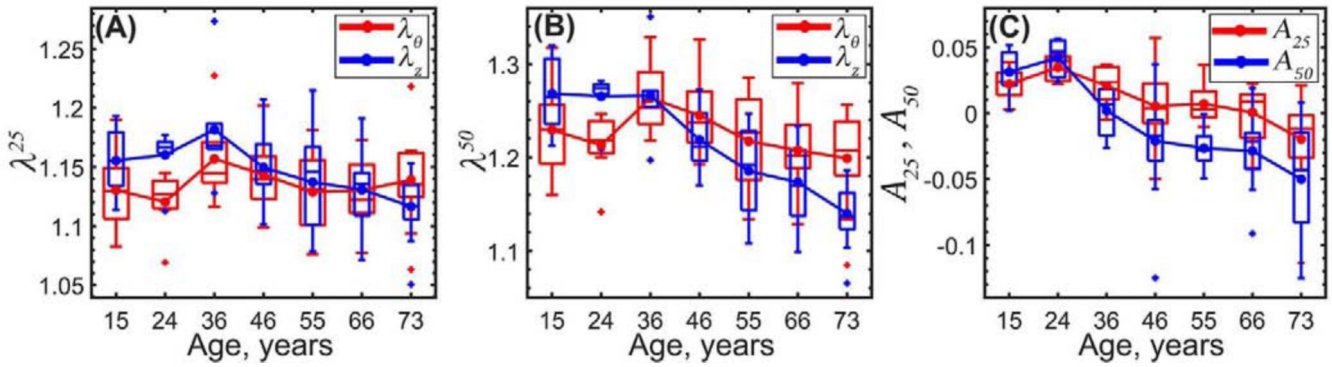

Figure 9:

Stretch corresponding to 25 *kPa,* λ^{25} (A) and 50 *kPa,* λ^{50} equibiaxial stress levels (B) in the circumferential (red) and longitudinal (blue) directions. (C) TA anisotropy at 25 *kPa*, A_{25} (red) and 50 *kPa*, A_{50} (blue) equibiaxial stress levels.

Author Manuscript Author Manuscript Author Manuscript Author Manuscript

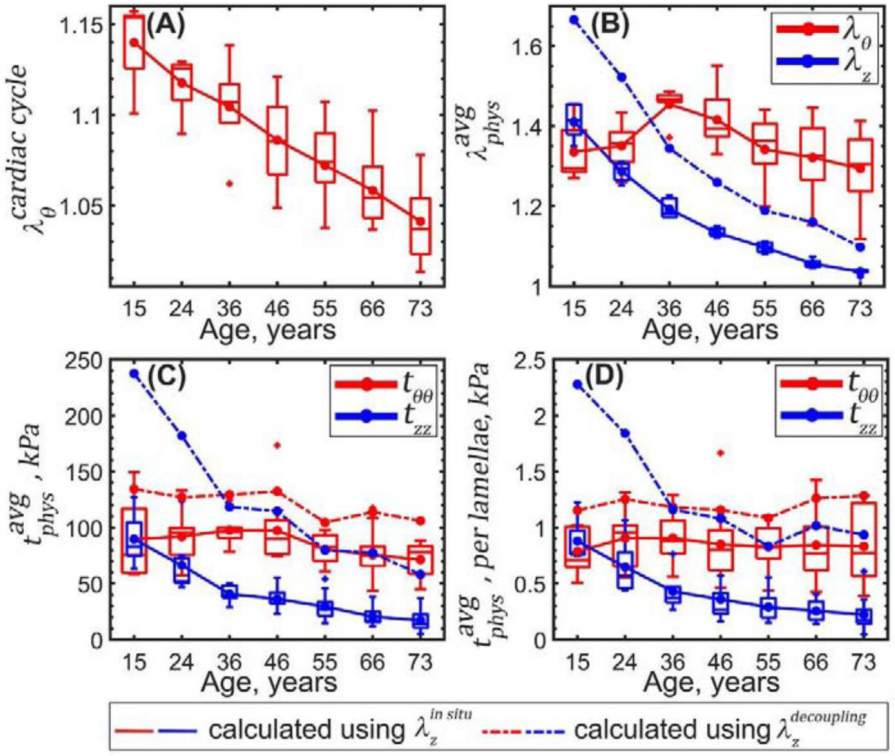

Figure 10:

Changes in the TA physiologic stress-stretch state with age. (A) Changes with age in stretch experienced during the cardiac cycle $\lambda_\theta^{cardiac\ cycle}$ from diastole (80 mmHg) to systole (120 mmHg). (B) Circumferential θ (red) and longitudinal z (blue) physiologic stretches λ_{phys}^{avg} and (C) stresses t_{phys}^{avg} at 100 mmHg calculated using *stress-free* state as a reference; and (D) average physiologic stress per elastic lamellae unit in the circumferential (red) and longitudinal (blue) directions determined using $\lambda_z^{in\ situ}$ (solid lines) and $\lambda_z^{decoupling}$ (dashed lines).

Author Manuscript Author Manuscript Author Manuscript Author Manuscript

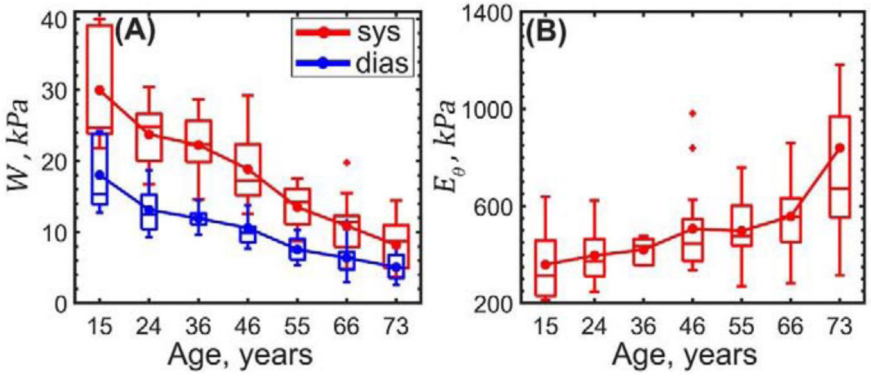

Figure 11:

Changes with age in the (A) stored elastic energy W at diastole (blue) and systole (red), and (B) physiologic circumferential stiffness E_θ.

Author Manuscript

Author Manuscript

Author Manuscript

Author Manuscript

Table 1:

Subject demographics and risk factors.

Age group (years)	n	Males, %	Current/Former smokers, %	BMI (average ± SD)	HTN, %	DM, %	Dyslipidemia, %	CAD, %
15.3 (13–20)	6	50	0/0	24.6±8.3	17	0	0	17
24.4 (21–30)	8	88	62/0	26.0±3.4	0	0	0	0
36.0 (31–40)	6	67	83/0	36.7±9.4	17	33	0	33
46.5 (41–50)	14	64	36/14	33.3±10.8	43	14	21	14
54.9 (51–60)	14	79	50/14	31.8±7.2	64	29	36	43
66.5 (61–70)	15	60	20/13	33.9±9.2	47	27	53	27
73.2 (71–78)	13	38	23/38	29.5±5.7	77	23	23	31

n: number of subjects in each age group, BMI: body mass index, HTN: hypertension, DM: diabetes mellitus, CAD: coronary artery disease

Author Manuscript Author Manuscript Author Manuscript Author Manuscript

Table 2:

Parameters for the neo-Hookean, Demiray (Delfino) and two-fiber family HGO models describing average responses of human TAs in 7 age groups. A total of 19 different loading protocols were used to determine constitutive parameters in these models.

	neo-Hookean model		Demiray (Delfino) model		
Age group (years)	μ, *kPa*	R^2	D_1, *kPa*	D_2	R^2
15.3 (13–20)	47.55	0.91	35.45	0.96	0.95
24.4 (21–30)	49.40	0.90	35.47	1.21	0.94
36.0 (31–40)	46.33	0.85	28.92	1.53	0.93
46.5 (41–50)	51.10	0.84	33.78	1.73	0.91
54.9 (51–60)	57.77	0.81	37.47	2.32	0.87
66.5 (61–70)	59.60	0.79	35.03	3.24	0.87
73.2 (71–78)	63.80	0.71	33.04	5.05	0.80
Two-fiber family HGO model					
Age group (years)	C_g, *kPa*	$C_1^1 = C_1^2$, *kPa*	$C_2^1 = C_2^2$	γ°	R^2
15.3 (13–20)	41.69	1.20	2.56	56.18	0.95
24.4 (21–30)	41.82	1.78	2.61	54.46	0.94
36.0 (31–40)	40.32	0.16	6.58	28.66	0.91
46.5 (41–50)	44.94	0.24	9.33	25.80	0.92
54.9 (51–60)	49.91	0.22	16.17	24.65	0.91
66.5 (61–70)	51.13	0.34	17.83	26.37	0.89
73.2 (71–78)	51.68	0.51	27.99	29.24	0.85

Author Manuscript
Author Manuscript
Author Manuscript
Author Manuscript

Table 3:

Parameters for the four-fiber family model describing average response of human TAs in 7 age groups. A total of 19 different loading protocols were used to determine constitutive parameters in this model. The coefficient of determination $R^2 \geq 0.99$ in all age groups.

Four-fiber family model								
Age group (years)	C_{gr}, *kPa*	$C_1^1 = C_1^2, kPa$	$C_2^1 = C_2^2$	C_1^3, kPa	C_2^3	C_1^4, kPa	C_2^4	γ°
15.3 (13–20)	14.99	12.61	0.57	25.78	0.00	18.57	0.00	45.29
24.4 (21–30)	13.99	13.89	0.83	31.74	0.00	15.60	0.23	41.80
36.0 (31–40)	11.71	11.17	1.45	22.29	0.16	8.00	1.41	38.41
46.5 (41–50)	14.32	9.56	2.72	24.75	0.19	14.48	2.00	38.41
54.9 (51–60)	15.60	9.26	5.35	28.53	0.37	12.69	4.80	37.83
66.5 (61–70)	13.94	9.66	6.87	29.03	0.39	16.24	5.38	40.70
73.2 (71–78)	12.67	6.87	14.86	25.63	1.19	13.88	11.86	39.55

Author Manuscript
Author Manuscript
Author Manuscript
Author Manuscript

Table 4:

Parameters for the four-fiber family constitutive model describing the response of human TAs in 7 age groups at the 25th percentile. Coefficient of determination $R^2 \geq 0.99$ for all age groups.

Four-fiber family model								
Age group (years)	C_g, *kPa*	$C_1^1 = C_1^2, kPa$	$C_2^1 = C_2^2$	C_1^3, kPa	C_2^3	C_1^4, kPa	C_2^4	γ°
15.3 (13–20)	11.45	38.68	0.00	0.17	0.03	32.65	0.00	62.08
24.4 (21–30)	16.22	13.53	0.92	31.10	0.00	11.77	0.69	43.98
36.0 (31–40)	19.25	8.75	2.97	22.40	0.20	0.01	14.09	31.82
46.5 (41–50)	16.69	13.25	2.50	27.17	0.26	15.52	2.64	40.24
54.9 (51–60)	25.62	10.96	10.77	34.98	0.36	7.60	13.25	33.19
66.5 (61–70)	21.54	4.75	15.71	29.18	0.64	21.84	8.65	41.51
73.2 (71–78)	27.33	1.69	31.27	11.18	4.17	5.17	29.59	43.03

Author Manuscript
Author Manuscript
Author Manuscript
Author Manuscript

Table 5:

Parameters for the four-fiber family constitutive model describing the response of human TAs in 7 age groups at the 75th percentile. Coefficient of determination $R^2 \geq 0.99$ for all age groups.

Four-fiber family model								
Age group (years)	C_g, *kPa*	$C_1^1 = C_1^2, kPa$	$C_2^1 = C_2^2$	C_1^3, kPa	C_2^3	C_1^4, kPa	C_2^4	γ°
15.3 (13–20)	13.82	10.31	0.00	21.90	0.01	13.90	0.00	43.95
24.4 (21–30)	10.45	14.69	0.59	29.16	0.00	15.60	0.00	39.85
36.0 (31–40)	9.09	12.10	0.77	20.56	0.00	16.83	0.13	40.23
46.5 (41–50)	14.40	6.66	2.91	20.17	0.29	9.98	1.74	35.42
54.9 (51–60)	15.99	6.17	3.77	17.52	0.50	7.75	3.57	39.44
66.5 (61–70)	11.33	8.05	4.67	24.53	0.43	17.08	2.66	41.37
73.2 (71–78)	5.04	7.55	8.44	30.53	0.15	28.06	3.80	40.52

Author Manuscript Author Manuscript Author Manuscript Author Manuscript

Table 6:

Parameters for the four-fiber family constitutive model describing the response of the most compliant human TA in each of the 7 age groups along with risk factors in these subjects. Coefficient of determination $R^2 \geq 0.99$ for all samples.

Four-fiber family model								
Risk Factors	C_{gr}, *kPa*	$C_1^1 = C_1^2, kPa$	$C_2^1 = C_2^2$	C_1^3, kPa	C_2^3	C_1^4, kPa	C_2^4	γ°
16y.o./ M/ BMI:25.2/ CAD	9.67	13.13	0.25	14.83	0.00	11.71	0.01	42.34
24y.o./ M/ BMI:25.1/ 5pky	9.28	23.79	0.24	29.52	0.01	2.87	0.00	32.91
32y.o./ M/ BMI:30/ 12pky	11.10	2.42	2.72	9.84	0.33	3.65	1.19	43.15
43y.o./ M/ BMI:21.9	11.68	16.72	0.75	18.80	0.00	17.01	0.12	41.98
51y.o./ M/ BMI:26.9/ HTN/ Dys/ 52pky	5.78	9.46	2.50	21.78	0.29	0.79	10.78	37.50
61y.o./ M/ BMI:39.1	5.84	14.85	1.37	23.46	0.00	11.92	2.81	40.63
73y.o./ F/ BMI:34.2/ HTN/86pky	6.54	14.42	6.79	23.88	0.00	3.11	8.38	36.61

y.o.: years old, M: male, F: female, BMI: body mass index, HTN: hypertension, DM: diabetes mellitus, CAD: coronary artery disease, Dys: Dyslipidemia, pky: pack-year history of cigarette smoking.

Author Manuscript

Author Manuscript

Author Manuscript

Author Manuscript

Table 7:

Parameters for the four-fiber family constitutive model describing the response of the stiffest human TA in each of the 7 age groups along with risk factors in these subjects. Coefficient of determination $R^2 \geq 0.99$ for all samples.

Four-fiber family model								
Risk Factors	C_{gr}, kPa	$C_1^1 = C_1^2, kPa$	$C_2^1 = C_2^2$	C_1^3, kPa	C_2^3	C_1^4, kPa	C_2^4	γ°
14y.o./ M/ BMI:22.1	28.08	21.23	0.35	36.71	0.00	7.17	0.00	37.07
23y.o./ M/ BMI:24.6/ 4pky	42.65	5.18	4.28	32.42	0.00	0.75	7.29	37.06
39y.o./ F/ BMI:40.2/ DM/ CAD/ 20pky	26.33	11.35	3.74	21.51	0.43	0.03	18.31	26.74
44y.o./ M/ BMI:33.2/ HTN	37.70	5.55	5.75	14.95	0.73	8.00	5.28	37.35
51y.o./ M/ BMI:29.1/ DM/ CAD/ 30pky	49.69	2.32	29.27	8.42	6.15	7.51	17.44	38.64
62y.o. / M/ BMI:47.3/ HTN/ DM/ Dys/ CAD	38.71	3.89	40.69	29.69	0.00	5.56	29.18	41.53
72y.o./ F/ BMI:20.5	29.13	21.52	75.85	39.08	20.29	45.98	40.29	43.27

y.o.: years old, M: male, F: female, BMI: body mass index, HTN: hypertension, DM: diabetes mellitus, CAD: coronary artery disease, Dys: Dyslipidemia, pky: pack-year history of cigarette smoking.